Geology and Scientific Significance of the Rümker Region in Northern Oceanus Procellarum: China's Chang'E-5 Landing Region

Y. Qian, L. Xiao, Y. Zhao, J. Huang, Jessica Flahaut, M. Martinot, J. Head, H. Hiesinger, Gang Wang

AGU100 ADVANCING EARTH AND SPACE SCIENCE

JGR

Journal of Geophysical Research: Planets

RESEARCH ARTICLE
10.1029/2018JE005595

Special Section:
Science and Exploration of the Moon, Near-Earth Asteroids, and the Moons of Mars

Geology and Scientific Significance of the Rümker Region in Northern Oceanus Procellarum: China's Chang'E-5 Landing Region

Y. Q. Qian[1], L. Xiao[1], S. Y. Zhao[1], J. N. Zhao[1], J. Huang[1], J. Flahaut[2,3], M. Martinot[4,5], J. W. Head[6], H. Hiesinger[7], and G. X. Wang[8]

[1]State Key Laboratory of Geological Processes and Mineral Resources, Planetary Science Institute, School of Earth Sciences, China University of Geosciences, Wuhan, China, [2]Centre de Recherches Pétrographiques et Géochimiques, CNRS/UMR 7358, Université de Lorraine, Vandœuvre-lès-Nancy, France, [3]Institut de Recherche en Astrophysique et Planétologie, CNRS/UMR 5277, Université Paul Sabatier, Toulouse, France, [4]Faculty of Science, Vrije Universiteit Amsterdam, Amsterdam, Netherlands, [5]Université Lyon 1, ENS-Lyon, CNRS, UMR 5276 LGL-TPE, Villeurbanne, France, [6]Department of Earth, Environmental and Planetary Sciences, Brown University, Providence, RI, USA, [7]Institut für Planetologie, Westfälische Wilhelms-Universität Münster, Münster, Germany, [8]Beijing Spacecrafts, China Academy of Space Technology, Beijing, China

Key Points:
- The Rümker region is located in the northwest of the Procellarum KREEP Terrane, experiencing a long and complex geological history
- We carried out a detailed geological study and defined and dated 14 geological units
- The Em4 is the science-richest unit and suitable for landing. It is proposed as the first priority for sample return

Supporting Information:
- Supporting Information S1
- Data Set S1
- Figure S1

Correspondence to:
L. Xiao,
longxiao@cug.edu.cn

Citation:
Qian, Y. Q., Xiao, L., Zhao, S. Y., Zhao, J. N., Huang, J., Flahaut, J., et al. (2018). Geology and scientific significance of the Rümker region in northern Oceanus Procellarum: China's Chang'E-5 landing region. *Journal of Geophysical Research: Planets*, *123*, 1407–1430. https://doi.org/10.1029/2018JE005595

Received 28 FEB 2018
Accepted 11 MAY 2018
Accepted article online 22 MAY 2018
Published online 12 JUN 2018

Abstract The Rümker region (41–45°N, 49–69°W) is located in northern Oceanus Procellarum of the Moon. Mons Rümker is the most distinctive geological feature in the area. The region is characterized by prolonged lunar volcanism (Late Imbrian Period to Eratosthenian Period), forming multiple geologic units in the area, including very low-Ti to low-Ti mare basalts, high-Ti mare basalts, and volcanic complexes. Each geologic unit has distinct element composition and mineral assemblages. The Rümker region, overlying the Procellarum KREEP Terrain, was selected as the landing region for China's Chang'E-5 lunar sample return mission. Prelanding analyses of the geologic context and scientific potential are reported in this contribution. We conducted detailed geological mapping using image, spectral, and altimetry data. Fourteen geological units were defined, a geologic map was constructed, and the geologic history was outlined. The western mare units (Im1, Im2, and Im3) are Imbrian-aged (~3.4–3.5 Ga) representing the major stage of lunar mare eruptive volcanism. The eastern young mare units (Em3 and Em4; <2 Ga) are among the youngest mare basalts on the Moon. They have never been explored in situ or studied in the laboratory. We suggest that samples returned from the eastern mare unit (Em4) could answer many fundamental questions and that this unit should be listed as the top priority landing site for Chang'E-5 sample return mission.

Plain Language Summary Recent studies find that the geological features and volcanic history of the Moon are far more complex than previously thought, and many of the most interesting areas have been neither explored nor sampled. One such area is the northern Oceanus Procellarum region which consists of very young (<2 Ga) mare materials and hosts one of the largest volcanic complexes on the Moon (Mons Rümker). To document the main themes in the geological history, we studied the Rümker region using a wide variety of lunar orbital data. Surface composition, mineralogy, morphology, and topography were used to create a geological map in which we identified 14 geological units. We found old Ti-poor basaltic units (similar to some Apollo samples) and very young unsampled Ti-rich basaltic units (<1.5 Ga). Samples from the young unsampled unit could answer many unresolved questions in lunar science because of its extremely young age. The area was selected as the landing region for China's Chang'E-5 lunar sample return mission in 2019. To maximize the scientific value of the returned samples, we assessed the scientific importance of each unit in our geologic map and suggest that the young mare basalt unit is the most valuable for sample return.

1. Introduction

The Procellarum KREEP Terrane (PKT) is one of the most prominent geochemically anomalous areas on the Moon (Haskin, 1998; Jolliff et al., 2000). It is characterized by high concentrations of heat producing elements (Th, U, and K; e.g., Haskin et al., 2000; Lawrence et al., 2000; Prettyman et al., 2006), a thin crust (Wieczorek et al., 2013), a complex thermal evolution history (Laneuville et al., 2013; Wieczorek & Phillips, 2000), and a long duration of lunar volcanism relative to most of the rest of the Moon (Hiesinger et al., 2000, 2003, 2010, 2011; Morota et al., 2011).

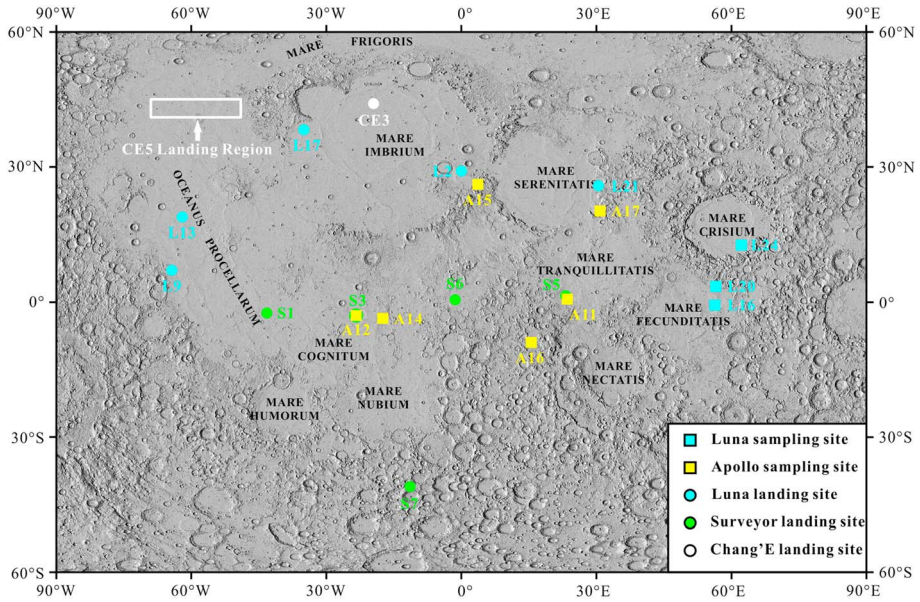

Figure 1. Location of the Rümker region and previous landing sites. The Rümker region is located in northern Oceanus Procellarum, away from previous sampling sites. The basemap is a Lunar Orbiter Laser Altimeter and Kaguya Terrain Camera merged hillshade map (simple cylindrical projection; Barker et al., 2016).

Located in northern Oceanus Procellarum (Figure 1), the Rümker region is in the northwest part of the PKT (Figure 2; Haskin, 1998; Jolliff et al., 2000). Its extended and complex geologic history includes multiple volcanic episodes, each differing in element composition and mineral assemblages (e.g., Hiesinger et al., 2003, 2011; Morota et al., 2011; Pieters, 1978; Zhang et al., 2016).

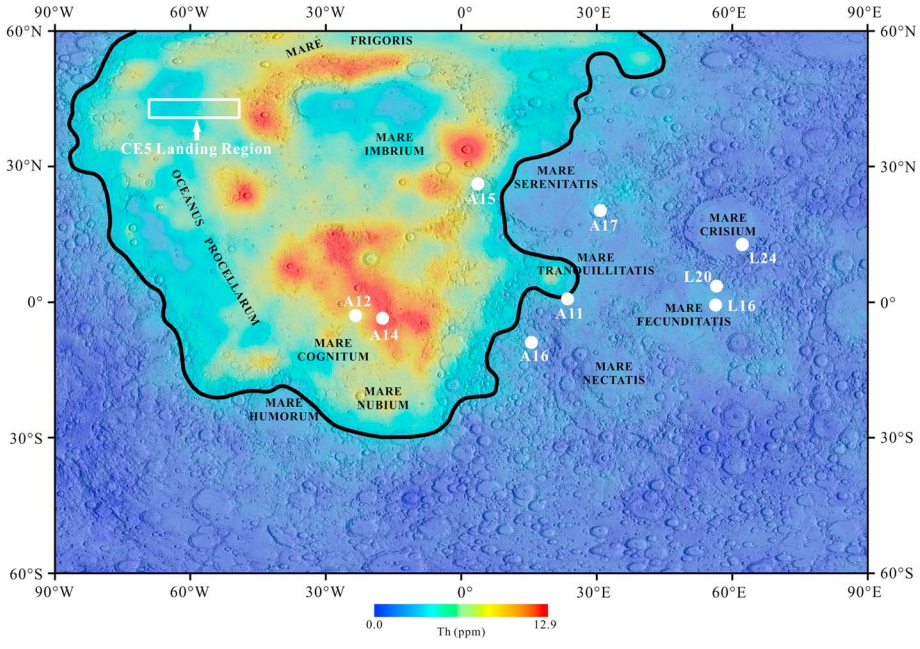

Figure 2. Thorium abundance map of the lunar nearside. The thick black line denotes the boundary of the Procellarum KREEP Terrane (Th $>$ 3.5 ppm). "A" represents the Apollo sampling sites; "L" represents the Luna sampling sites. The white box indicates the CE5 designated landing region. The basemap is a Lunar Orbiter Laser Altimeter and Kaguya Terrane Camera merged hillshade map (Barker et al., 2016) superposed on the Lunar Prospector thorium data (Prettyman et al., 2006).

Earliest geological mapping (Wilhelms & McCauley, 1971; 1:5 million) defined two mare units in the Rümker region, that is, Imbrian-aged and Eratosthenian-aged mare units (Im and Em). Scott et al. (1977) combined these into an Imbrian-Eratosthenian-aged mare unit (EIm). Scott and Eggleton (1973) subdivided two non-mare units (Ith and If) and two mare units (Im and Em) in their 1:1 million geological map. The authors concluded that the Ith unit resembles the Alpes Formation and that the If unit is part of the Fra Mauro Formation, both of which are interpreted as ejecta materials from the Imbrium impact basin (Page, 1970; Scott & Eggleton, 1973).

Whitford-Stark and Head (1980) later subdivided four lithostratigraphic formations in Oceanus Procellarum according to surface morphology and spectral characteristics. Three of them occur in the Rümker region, including the Telemann Formation (the western part), the Sharp Formation (the eastern part), and the Hermann Formation (the central southern part). Three basalt end-members were identified (Dechen Basalt, Lavoisier Basalt, and Roris Basalt), and their sources and emplacement styles were studied in detail (Whitford-Stark & Head, 1980).

More recent stratigraphic works were based on Clementine data. Hiesinger et al. (2003, 2011) used Clementine color ratio data (750–400 nm/750 + 400 nm as red, 750/990 nm as green, and 400/750 nm as blue) to map the mare units in Oceanus Procellarum. Three spectrally homogeneous units in the Rümker region were defined and dated by crater size-frequency distribution (CSFD) methods (P9, 3.47 Ga; P10, 3.44 Ga; P58, 1.33 Ga; Hiesinger et al., 2003, 2011). Using Clementine false-color mosaics (750 nm/415 nm as red, 750 nm/950 nm as green, and 415 nm/750 nm as blue), titanium and iron data, Boroughs and Spudis (2001) mapped six lava flows in northern Oceanus Procellarum. Four of them are located within the Rümker region (Flow2, Flow3, Flow5, and Flow6).

Mons Rümker (i.e., Rümker Hills), the most distinctive topographic feature in northern Oceanus Procellarum, has long been recognized as one of the three major volcanic complexes in Oceanus Procellarum (Whitford-Stark & Head, 1977). Its morphology, composition, mineralogy, and formation mechanism have been well studied (Campbell et al., 2009; Dmitrovsky et al., 2017; Farrand et al., 2015; Smith, 1974; Whitford-Stark & Head, 1977; Wöhler et al., 2007; Zhao et al., 2017). A comprehensive analysis using recent lunar orbital data (Zhao et al., 2017) identified three geologic units at Mons Rümker and further obtained their model ages by CSFD methods (IR1, 3.71 Ga; IR2, 3.58 Ga; IR3, 3.51 Ga). Zhao et al. (2017) concluded that the steep-sided domes and shallow domes on Mons Rümker are probably formed at different stages of evolution of this volcanic complex.

China's first lunar sample return mission, Chang'E-5 (CE5) mission, is scheduled to launch in 2019, following the successful Chang'E-3 (CE3) soft landing and roving exploration of northern Mare Imbrium (44.12°N, 19.51°W; Ling et al., 2015; Xiao, 2014; Xiao et al., 2015; Zou et al., 2016). The Rümker region in northern Oceanus Procellarum (41–45°N, 49–69°W, ~58,000 km^2 in area) is the landing region selected for the CE5 mission (Zeng et al., 2017). Up to 2 kg of lunar samples from the surface and subsurface (up to 2 m in depth) are planned to be collected and returned to the Earth (Wang & Xiao, 2017; Zou & Li, 2017), providing an opportunity to study new lunar samples in terrestrial laboratories since Luna-24 (1976).

The Rümker region remains unexplored by robotic or human landing missions carried out earlier by the United States (Surveyor, Apollo) or the Soviet Union (Luna), and no samples have ever been returned from this broad area (Figures 1 and 2). Understanding its geological context and evaluating the scientific value of materials from this region are key to the further exploration and preparation for sample return and analysis. A detailed study of Mons Rümker was carried out, and several candidate landing sites were proposed by Zhao et al. (2017). However, the extensive mare areas to the north, making up the majority of the landing region (Figure 3), have not been well studied using newly obtained orbital remote sensing data. Therefore, the goals of this study are (1) to characterize the geological context of the Rümker region, (2) to assess their science potential for understanding and resolving outstanding lunar science questions, and (3) to propose the most scientifically significant landing and sampling sites for the CE5 mission. To understand better the context of the Rümker region, we extend our study area to 39–46°N, 48–70°W (Figure 3).

2. Data and Methods

2.1. Topography and Geomorphology

A Kaguya Terrain Camera (TC) global image mosaic with uniform morning illumination (TC Morning Map data) and TC DTM data, with a spatial resolution of ~10 m/pixel (Haruyama et al., 2008, 2014), were

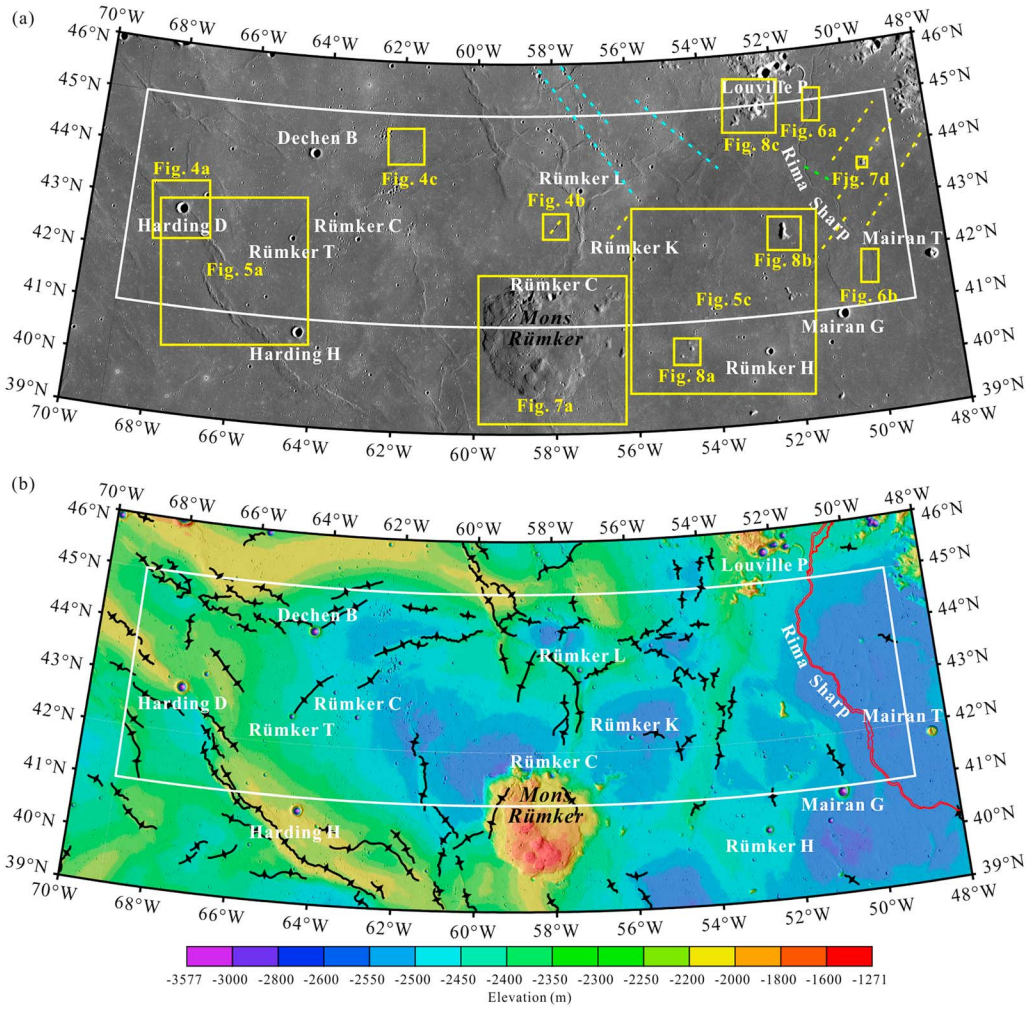

Figure 3. (a) Terrane camera (TC) morning map of the Rümker region (Lambert conformal conic projection). The white box denotes the CE5 landing region. The yellow boxes represent the locations of other figures in this paper. The yellow dashed lines denote the ejecta from Harpalus carter. The blue dashed lines denote ejecta from Pythagoras crater. The green dashed lines denote ejecta probably from Copernicus crater. (b) Topography of the Rümker region. The image is a Lunar Orbiter Laser Altimeter and Kaguya TC merged hillshade map superposed on the TC DTM data (Lambert conformal conic projection). The white box denotes the CE5 landing region. The black lines denote wrinkle ridges. The red lines denote Rima Sharp.

mosaicked to analyze topographic and geomorphologic features. TC Morning Map data were used to perform the CSFD measurements on the major mare units to determine their absolute model ages. TC Morning Map and TC DTM data were downloaded from the SELENE Data Archive (http://darts.isas.jaxa.jp/planet/pdap/selene/). Lunar Reconnaissance Orbiter (LRO) wide-angle camera (WAC) DTM data (~118 m/pixel; Scholten et al., 2012) were applied at a baseline length of 354 m to survey surface slopes. LRO narrow-angle camera (NAC) data were used for more detailed studies of local features, due to their high spatial resolution (up to ~0.5 m/pixel) and more variable illumination conditions (Robinson et al., 2010). WAC DTM data and NAC data were downloaded from the LROC website (http://lroc.sese.asu.edu/).

2.2. Composition

2.2.1. TiO_2 and FeO Contents

Kaguya Multiband Imager (MI) data were downloaded from the SELENE Data Archive (http://darts.isas.jaxa.jp/planet/pdap/selene/). MI has five visible bands (415, 750, 900, 950, and 1,000 nm) and a spatial resolution of

20 m (Ohtake et al., 2008). TiO_2 and FeO abundances were calculated from MI data using the algorithms described by Otake et al. (2012):

$$\theta_{Ti} = \arctan\{[(R_{415}/R_{750}) - 0.208]/(R_{750} + 0.108)\} \quad (1)$$

$$\text{wt\%TiO}_2 = 0.72 * \theta_{Ti}^{14.964} \quad (2)$$

$$\theta_{Fe} = \arctan\{[(R_{950}/R_{750}) - 1.250]/(R_{750} - 0.037)\} \quad (3)$$

$$\text{wt\%FeO} = 20.527 * \theta_{Fe} - 12.266 \quad (4)$$

where R_{415}, R_{750}, and R_{950} are the reflectance at each corresponding band. The standard deviation of the TiO_2 and FeO contents are 0.43 and 0.81 wt %, respectively. Caution should be exercised in interpretations when the TiO_2 content is lower than 2 wt %, at which point the linear correlation between UV/VIS (321 nm/415 nm) and TiO_2 content tends to break down (Coman et al., 2018; Sato et al., 2017).

A false color composite map was produced from MI data by assigning 750 nm/415 nm as red, 750 nm/950 nm as green, and 415 nm/750 nm as blue (Pieters et al., 1994). Because of its sensitivity to surface maturity and composition, and its ability to highlight subtle spectral differences (Eliason et al., 1999; Pieters et al., 1994), the false color composite map, together with titanium and iron variation and crater distribution data, was used to determine the nature and boundaries of geologic units.

2.2.2. Mineralogy

Moon Mineralogy Mapper (M^3) reflectance data acquired from the optical period OP2C were selected because of their full spatial coverage over the Rümker region. M^3 OP2C data have a spatial resolution of 280 m/pixel, with 85 bands, spanning from 430 to 3,000 nm (Pieters et al., 2009). The M^3 data used in this study are calibrated data archived in the Planetary Data System (version 1 of Level 2), radiometrically corrected (Green et al., 2011), geometrically corrected (Boardman et al., 2011), thermally corrected (Clark et al., 2011), and photometrically corrected (Besse et al., 2013).

To decrease the effects of space weathering and to permit a more robust spectral study, we removed the continuum following the method of Horgan et al. (2014) and Martinot et al. (2018). These authors defined the continuum by maximizing the 1 and 2 micron absorption bands. Spectral parameters such as band centers, band depths, band areas, and band asymmetries were calculated for the 1 and 2 micron absorption bands of each spectrum. M^3 RGB composite maps using these criteria were produced to highlight the mineralogical diversity of the Rümker region (Martinot et al., 2018; Mustard et al., 2011). Both M^3 original and continuum-removed spectra were visually analyzed for definitive mineral identification, performed by comparison of the M^3 spectra with the RELAB reference library (http://www.planetary.brown.edu/relab/).

3. Results

3.1. Topography

The Rümker region is located within the relatively smooth mare plains of northern Oceanus Procellarum (Kreslavsky et al., 2013; Rosenburg et al., 2011; Figure 3a). This area is covered by widespread mare basalts and is generally flat. The mean slope of the area is 1.1° (at a baseline length of 354 m), with only 10% of the area exceeding a slope of 2°. The average elevation of the mare area is ~−2,145 m. The western maria is 200–300 m higher than the eastern maria (Figure 3b). The highest point is in the south of Mons Rümker (−1,271 m), and the lowest point is at the bottom of Mairan G crater (−3,571 m). The regional topography is largely influenced by mare ridges, along which the mare surface is locally raised, up to 100–200 m. Mons Rümker, ~70 km in diameter, stands up to 1,300 m above the surrounding mare. It has a mean slope of 2.7°. The individual domes on Mons Rümker are slightly steeper than the plateau.

3.2. Geomorphology

3.2.1. Impact Craters

Most of the craters in the area are simple primary craters smaller than 2 km in diameter, characterized by bowl-shaped floors, only few with flat bottoms. Almost all craters larger than 2 km in diameter are found in the western maria. It is also apparent that the western maria has a much higher crater density than the eastern maria. Harding D (centered at 42.8°N, 67.6°W; Figure 4a) is the largest crater in the area. It has a

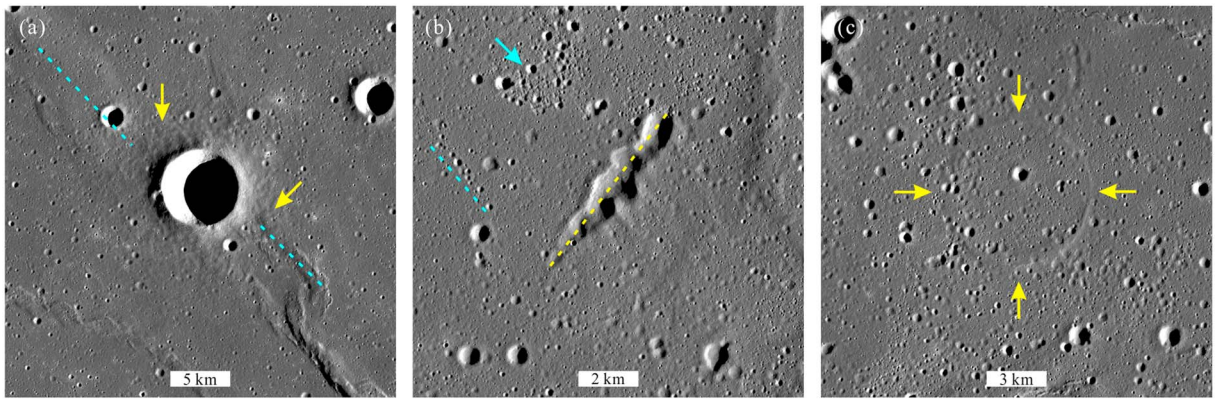

Figure 4. Typical impact crater-related structures in the Rümker region. (a) Harding D crater (centered at 42.8°N, 67.6°W; Figure 3a). This crater formed on a NW-oriented wrinkle ridge (blue dashed lines). Its ejecta (yellow arrow) buries a portion of the wrinkle ridge. (b) Secondary crater clusters (centered at 42.9°N, 58.0°W; Figure 3a). The yellow dashed line denotes Harpalus secondaries (Scott & Eggleton, 1973). The secondary craters denoted by the blue dashed line are radial to Copernicus crater and are thus probably formed by Copernicus crater ejecta. The blue arrow denotes secondaries without any dominant orientations. (c) A buried crater (centered at 44.4°N, 61.9°W; Figure 3a). The yellow arrows denote the exposed rim crest of the preexisting crater. This preexisting crater is almost completely buried by the later lavas. The subsequent lava flooding is estimated to be less than ~800 m, using the depth/diameter relationships of fresh craters (Pike, 1974).

diameter of 6.3 km and a bowl-shaped floor. Its rim is ~250 m higher than the surrounding mare. This crater formed on a NE-orientated wrinkle ridge.

Secondary crater clusters formed by ejecta from the crater Copernicus (NW trend), Harpalus (NE trend), and Pythagoras (NW trend) are distributed in the area (Figure 3a; Scott & Eggleton, 1973). For example, the NE-oriented clusters to the north of Mons Rümker are formed by Harpalus crater ejecta (Figure 4b; Scott & Eggleton, 1973). However, the sources of the secondaries that are not characterized by any preferred orientations are mostly unknown.

There are at least 35 buried craters in the study area (39–46°N, 48–70°W) and 15 buried craters that lie within the Rümker region (41–45°N, 49–69°W), mostly in the eastern maria. These premare craters were partially filled by lava flows, leaving only the raised rim crests visible on the surface (Figure 4c).

3.2.2. Wrinkle Ridges

Lunar wrinkle ridges are abundant in the study area (Figure 3b). Most of the wrinkle ridges have typical shapes as described by Strom (1972) and Sharpton and Head (1988) (i.e., a gently sloping, broad arch at the base, and a sharper but irregular ridge at the top; Figure 5). The dimensions of the wrinkle ridges are variable in the Rümker region. In the western maria, the wrinkle ridges range up to 6 km in width and 110 km in length and are 200 m above the surrounding mare. In the eastern maria, the wrinkle ridges are smaller than those in the western maria, mostly less than 1.5 km in width and 20 km in length, and are seldom much higher than 50 m above the surrounding mare.

The wrinkle ridges in the Rümker region have three preferred orientations (NW, NNW, and NE, respectively). In the western maria, most wrinkle ridges are oriented NW or NNW, consistent with the preferred orientation of those in Oceanus Procellarum as a whole (Yue et al., 2015). For example, the wrinkle ridges between Harding D and Harding H craters in the western maria are parallel and have a distinct NW trend (Figure 5a). Five independent wrinkle ridges are parallel with each other, with variable lengths (10 to 100 km) but similar morphologies and slopes. In the vicinity of these parallel wrinkle ridges, a linear fault vertically cuts a wrinkle ridge (Figure 5b).

In the eastern maria, the wrinkle ridges have a prominent NE trend along the outer ring of the Imbrium basin marked by the shoreline of Mare Frigoris (Spudis et al., 1988; Wilhelms & McCauley, 1971). This trend suggests that the wrinkle ridge formation in the eastern maria was affected by the ring system of the Imbrium basin (Head, 1982; Maxwell et al., 1975).

3.2.3. Sinuous Rilles

In the eastern maria, a sinuous rille (Rima Sharp) is incised into the mare plains along the mare/highland boundary (Figure 3b). Rima Sharp is even the longest sinuous rille on the Moon (Hurwitz et al., 2013). It

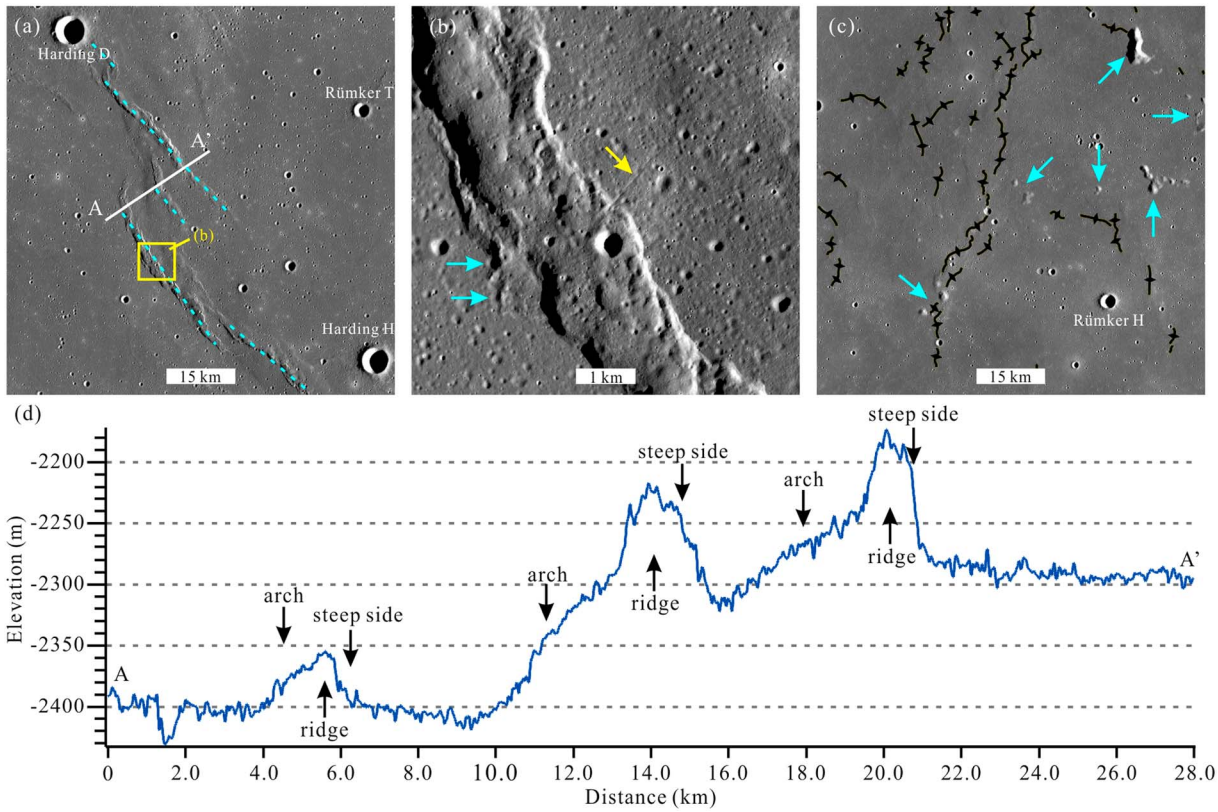

Figure 5. Wrinkle ridges. (a) NW-orientated parallel wrinkle ridges (centered at 41.7°N, 66.3°W; Figure 3a). The blue dashed lines denote parallel wrinkle ridges. AA′ shows the location of the profile in Figure 5d. The yellow box denotes the location of Figure 5b. (b) A southwest trending fault cuts the wrinkle ridge in the area (the yellow arrow). The craters denoted by blue arrows are cross-cut by the ridge front. (c) Wrinkle ridges in the eastern maria (centered at 41.3°N, 53.9°W; Figure 3a). They are oriented NE along the outer ring marked by kipukas (see section 3.2.5). (d) Topographic profile across wrinkle ridges (AA′ in (a)). The wrinkle ridges in the area display the typical broad arches (2–3°) and sharp ridges (up to 8°; Sharpton & Head, 1988; Strom, 1972).

originates in Sinus Roris, to the north of the Rümker region, at an elevation of −2,300 m, and fades into the mare surface to the south at an elevation of −2,500 m (Figure 6). Rima Sharp is 566 km long, 257 km of which are within the study area. The width of Rima Sharp varies from 0.8 to 3 km. Its depth varies from 20 to 50 m, and the narrowest parts of the channel have greater depths than those of the wider parts. The channel wall slopes of Rima Sharp fluctuate between 8 and 12°. The regional slope of Rima Sharp (defined as the gradient of the material surrounding the sinuous rille) is −0.02° as measured by Hurwitz et al. (2013). A thermal erosion formation mechanism is favored for such sinuous rilles (Hurwitz et al., 2012).

3.2.4. Volcanic Domes

Volcanic domes are relatively common in the lunar maria (Head & Gifford, 1980; Smith, 1973). They are often observed in clusters, as in the case of Mons Rümker (Smith, 1974; Whitford-Stark & Head, 1977), where most of the volcanic domes in the study area are located. Zhao et al. (2017) identified 22 volcanic domes on the Rümker plateau and divided them into two groups: steep-sided domes and shallow domes (Figure 7a). The steep-sided domes usually have relatively steep flank slopes (>5°) and greater heights, with associated volcanic features such as possible summit pits and flow features (Figure 7b). The shallow domes have gentle topographic relief and lower heights (<200 m); only two domes have associated volcanic features. Both dome groups are interpreted to have formed by extrusion of basaltic magma to form small shield volcanoes similar to those in Marius Hills (Head & Gifford, 1980; Head & Wilson, 2017; Lawrence et al., 2013; Zhao et al., 2017).

Another possible volcanic dome (named East Dome in this study; 49.85°W, 43.68°N) is located near the Mairan domes, close to the mare/highland boundary. The East Dome is circular in shape (Figure 7d), with a diameter of ~3 km, and is up to 205 m higher than the mare (Figure 7e). The flank slope is up to 9°, less than those of the

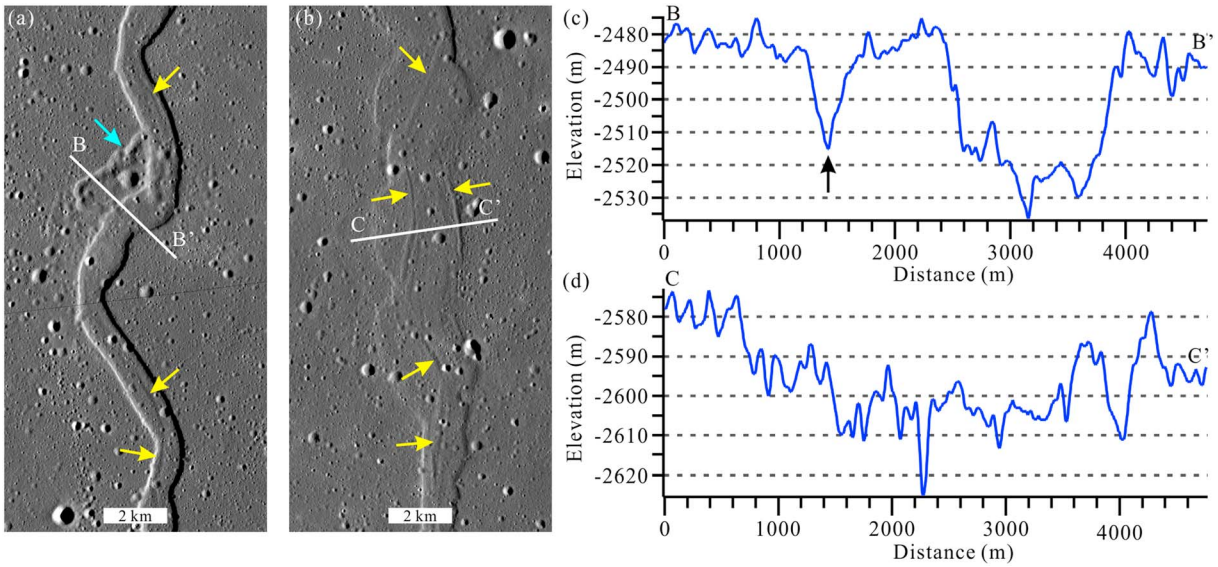

Figure 6. Sinuous rilles. (a) The narrow and deep parts of Rima Sharp (centered at 45.0°N, 51.0°W; Figure 3a). Rima Sharp is ~1.3 km wide and 40–50 m deep in this part. The yellow arrows denote small channels within Rima Sharp. The blue arrow denotes a shallow (~30 m in depth) branch of Rima Sharp. The white line (BB′) shows the location of the profile in Figure 6c. (b) The wide and shallow part of Rima Sharp (centered at 41.7°N, 50.0°W; Figure 3a). Rima Sharp is ~3.1 km wide and ~20 m deep in this part. The yellow arrows denote small channels within Rima sharp. The white line (CC′) shows the location of the profile in Figure 6d. (c) Topographic profile of the narrow part of Rima Sharp. The black arrow denotes a branch of Rima Sharp. (d) Topographic profile of the wide part of Rima Sharp.

Mairan domes (Glotch et al., 2011; Head & McCord, 1978). This dome is cratered, but most of the craters appear to be fresh secondaries that not highly degraded. A circular depression (~1.3 km in diameter) which may be a volcanic depression is outlined in the northwest (the yellow dashed line in Figure 7d). The East Dome was first described as a silica-rich dome by Glotch et al. (2011). Similar features in the vicinity

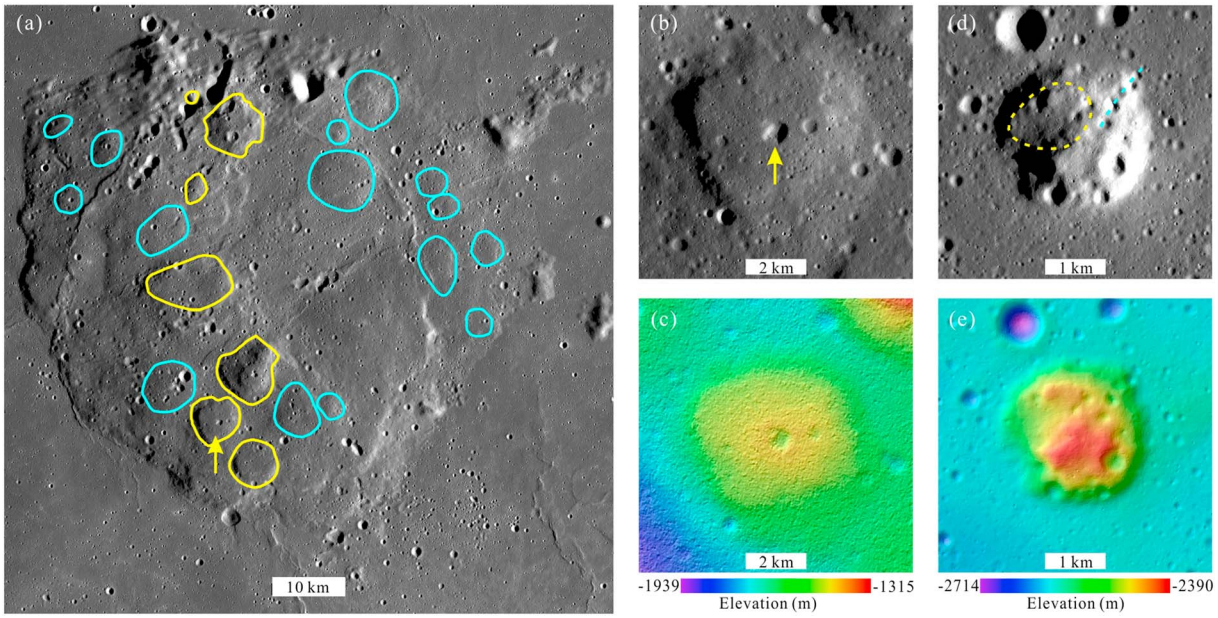

Figure 7. Volcanic domes in the Rümker region. (a) Volcanic domes on Mons Rümker. The yellow lines denote steep-sided domes (flank slopes >5°). The blue lines denote shallow domes (flank slopes <5°). The yellow arrow denotes the steep-sided dome in Figure 7b. (b) Steep-sided dome in the southwest of Mons Rümker. The yellow arrow denotes a summit pit, which may be a volcanic crater (Zhao et al., 2017). (c) Topography of the steep-sided dome in Figure 7b. The image is a Lunar Orbiter Laser Altimeter and Kaguya Terrane Camera (TC) merged hillshade map superposed on TC DTM data. (d) The East Dome (centered at 49.85°W, 43.68°N; Figure 3a). The yellow dashed line denotes a circular structure that may be a volcanic depression. The blue line denotes NE trending secondary craters. (e) Topography of the volcanic dome in Figure 7d. The image is a narrow-angle camera (NAC) hillshade map superposed on NAC DTM data.

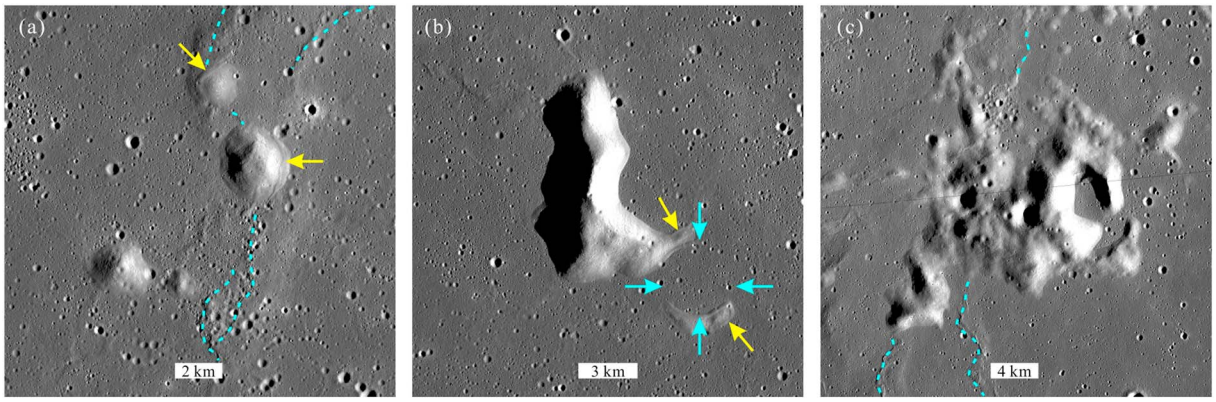

Figure 8. Kipukas in the Rümker region. (a) Isolated kipukas (centered at 40.4°N, 54.8°W; Figure 3a). These kipukas are reshaped by wrinkle ridges (the blue dashed lines), especially in the places denoted by the yellow arrows. (b) The largest isolated kipuka (centered at 42.6°N, 52.1°W; Figure 3a). The yellow arrows denote debris. The blue arrows denote a buried crater (~3.9 km in diameter). (c) Highlands near Louville P crater, with a morphology that is similar to the kipukas scattered in the eastern maria. The blue dashed lines denote wrinkle ridges.

(the Gruithuisen and Mairan domes) are interpreted to have formed from high viscosity silica-rich magmas of rhyolitic or dacitic composition (Glotch et al., 2010, 2011; Head & Wilson, 2017; Ivanov et al., 2016; Wilson & Head, 2003).

3.2.5. Kipukas

Kipukas are islands or exposures of earlier structures or units that have been surrounded by later units. Numerous isolated kipukas are identified within the eastern maria. They are hilly to hummocky highland materials of various shapes and are up to 500 m higher than the surrounding surface. The kipukas have relatively smooth surfaces with fewer craters than the maria, and the few remaining craters are all heavily degraded (Figures 8a and 8b). At the base of the kipukas, debris from the upper slopes encircles the kipukas and forms a 200 to 300-m wide deposit zone (Head, 1977). Although the kipukas usually display a scattered distribution in the eastern maria, the highlands in the northeastern part of the study area near Louville P crater have similar morphologies (Figure 8c). Both the isolated kipukas and highlands near Louville P crater are characterized by subdued shapes and heavily degraded superposed craters, lying on the possible Imbrium basin ring (Wilhelms & McCauley, 1971).

3.3. Composition

3.3.1. TiO_2 and FeO Concentrations

TiO_2 and FeO abundance maps (Figure 9) were used to estimate the surface TiO_2 and FeO contents. The results show that both the TiO_2 and FeO abundances vary significantly across the area. The TiO_2 contents range up to 7.5 wt % (Figure 9a), and the FeO contents vary from 10 to 18.0 wt % (Figure 9b). The western and the eastern maria are dominated by two different types of mare basalts, with distinctly different TiO_2 contents, and varying FeO contents. However, it should be noted that about 45% of the study area has TiO_2 contents lower than 2 wt %, a value at which the specific TiO_2 contents are probably not accurate (Coman et al., 2018).

The western maria are characterized by very low-Ti to low-Ti basalts (up to 5.0 wt %, TiO_2 content; Neal & Taylor, 1992). The mean content of TiO_2 is 1.6 wt %. About 80% of the area has TiO_2 contents lower than 1%. The northwestern part of the western maria exhibits the lowest TiO_2 contents in the study area (1.3 wt %, mean content). The TiO_2 contents increase from north to south in the western maria and reach an average of 2.4 wt % to the south of Harding D crater. The FeO contents of the western maria are lower than of the eastern maria. The FeO contents range from 14 to 17 wt % (15.8 wt %, mean content), increasing toward the south.

A very low-FeO zone occurs in the northeast of the western maria, without variation of TiO_2 abundances, suggesting an origin due to the emplacement of ejecta from Pythagoras crater (low-Fe and very low-Ti), rather than due to the composition of local bedrock or regolith. Large craters and their surrounding ejecta in the western maria have even lower TiO_2 contents than the mare surface ($<$1 wt %); we interpret this to be due

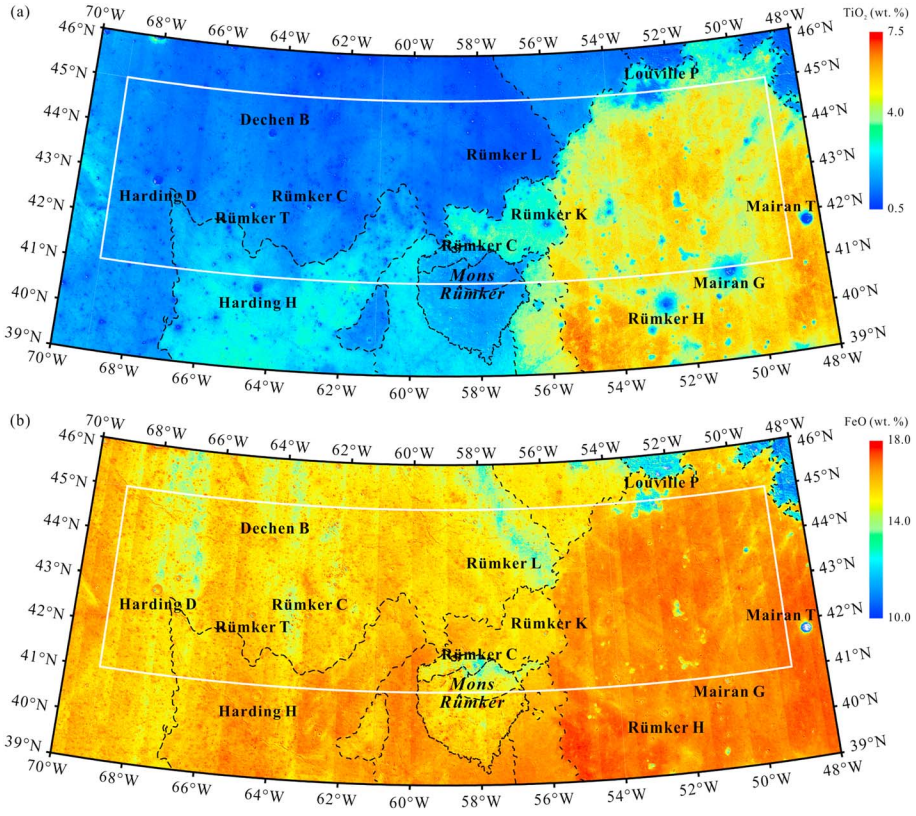

Figure 9. TiO_2 and FeO abundance maps of the Rümker region (Lambert conformal conic projection). (a) TiO_2 abundance map of the study area. (b) FeO abundance map of the study area. The white boxes denote the CE5 landing region. The black dashed lines denote geologic boundaries discussed in section 3.4.

to the excavation of underlying very low-Ti lava flows or underlying fresh rocks of the same lithology. This relationship between lava flows and their compositions can be used to obtain the thickness of lava flows (Thomson et al., 2009; Weider et al., 2010), which is discussed in section 4.1.1.

The eastern maria are clearly more enriched in TiO_2 (4.7 wt %, mean content) and FeO (16.7 wt %, mean content) than the western maria. About 65% of the eastern area has TiO_2 contents between 4 and 7 wt % and about 80% of the area has FeO contents greater than 16%. Most of the eastern maria are covered by bright (high albedo) ray materials radiating from Copernican-aged Harpalus crater (Figure 3a), whose bedrock target is low-Ti mare basalts. These materials clearly decrease the surface TiO_2 contents in the eastern maria. Except for these areas covered by ejecta, rocks in the region are classified as high-Ti basalts (TiO_2 contents between 6 and 7 wt %; Neal & Taylor, 1992).

The underlying older low-Ti materials are clearly excavated by superposed impact craters, as shown in the nature of the ejecta from relatively large and fresh craters. This ejecta has TiO_2 contents close to those of the western maria (1.9 wt %, mean content). The kipukas are expected to show very low TiO_2 and FeO contents due to their origin as highlands (Spudis et al., 1988), but mixture with the surrounding high-Ti basalts by impacts has commonly raised their titanium and iron abundance.

Mons Rümker is dominated by low-Ti basalts (1.8 wt %, mean content; Neal & Taylor, 1992). The mean content of FeO is 15.6 wt %. The FeO content is lower in the northeastern Rümker plateau, due to admixing of highland and basaltic materials (Zhao et al., 2017).

3.3.2. Mineralogy

The color composite maps shown in Figure 10 highlight the presence of distinct spectral units, represented by different colors. The area is dominated by pyroxene signatures, characterized by broad absorption bands centered around 1 and 2 microns (Adams, 1974). Other common lunar minerals such as olivine or plagioclase

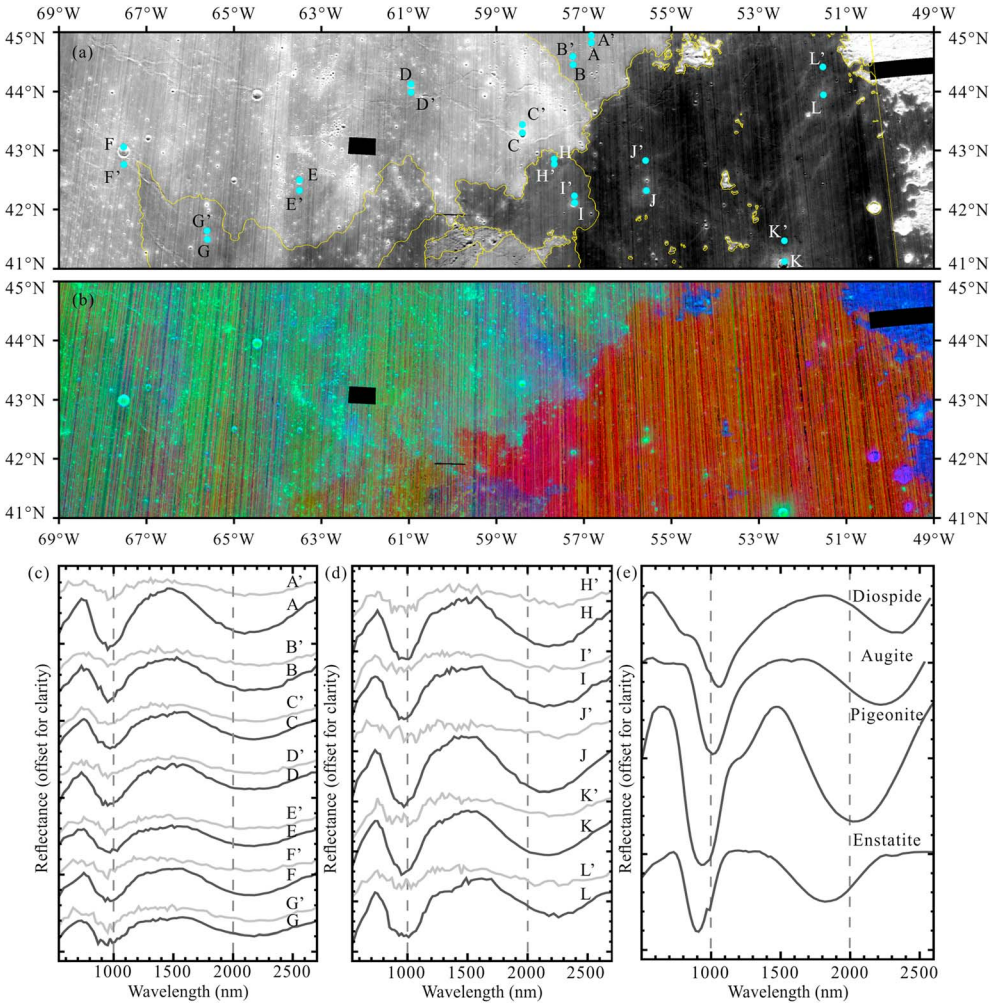

Figure 10. M^3 spectral analysis of the Rümker region. (a) M^3 2,900-nm mosaic. (b) M^3 RGB composite of spectral parameters (R = 2 micron band center, stretched values: 2,000–2,500 nm; G = 2 micron band depth, stretched values: 0.04–0.13; B = reflectance at 1,580 nm, stretched values: 0.085–0.15). (c) M^3 continuum-removed 3 × 3 pixel average spectra (using methods of Martinot et al., 2018) of selected impact craters (A through G) and of nearby maria (A′ through G′) within the western maria (see positions on Figure 10a). (d) M^3 continuum-removed 3 × 3 pixel average spectra of selected impact craters (H through L) and of the nearby maria (H′ through L′) within the eastern mare (see positions on Figure 10a). (e) RELAB database pyroxene spectra processed using the method of Martinot et al. (2018) (respective samples RELAB-ID: PD-CMP-006, AG-TJM-010, DL-CMP-008, and DH-MBW-005 for diopside, augite, pigeonite, and enstatite).

have not been detected throughout the study area. Although several parameters, such as surface physical properties and rock texture, may also influence the band shape, band center positions are often indicative of the pyroxene cation content (Adams, 1974; Burns et al., 1973; Cloutis & Gaffey, 1991).

The western maria spectra (Figure 10c) are characterized by greater band depths and band centers at shorter wavelengths than the eastern maria spectra. Spectra from the eastern maria (Figure 10d) are quite homogenous, with the exception of those taken from the interiors of impact craters with diameters exceeding 900 m, where the spectra have band centers located at shorter wavelengths, consistent with the western maria spectra. It is therefore likely that the impact craters of the eastern maria have excavated material from an older, buried unit, spectrally similar to the western maria. Spectra of the western maria show 1 and 2 micron bands centered around 990 and 2,180 nm, consistent with a pyroxene of intermediate-Ca composition such as pigeonite (Figure 10e). Spectra of the eastern maria have 1 and 2 micron bands centered at ~1,010 and 2,260 nm, consistent with high-Ca pyroxene such as augite (Figure 10e). Ling et al. (2017) also conducted

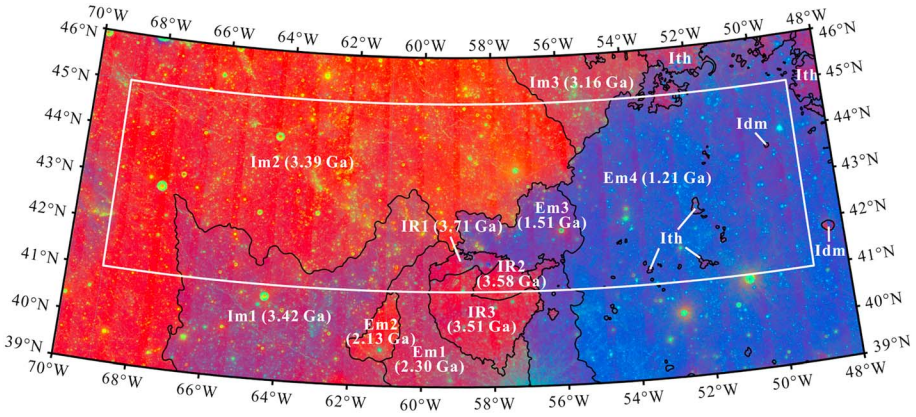

Figure 11. Geologic units of the Rümker region. The black lines denote the geological boundaries. The white box denotes the CE5 landing region. Im1, Im2, and Im3 are Imbrian-aged mare units. Em1, Em2, Em3, and Em4 are Eratosthenian-aged mare units. IR1, IR2, and IR3 are Rümker plateau units. Ith is a highland unit. Idm is an Imbrian-aged dome unit.

spectral observation of the Rümker region. Both Ling et al. (2017) and this survey suggest that there is little low-Ca pyroxenes in the mare area.

Mons Rümker, the Mairan T dome, and the highlands in Montes Jura to the east of the study area are all characterized by weaker pyroxene absorptions bands, which likely indicate a lower mafic component, or more mature regolith (Fischer & Pieters, 1994). The pyroxene component of the highlands is slightly more variable, with absorption bands shifted toward shorter wavelengths (~950 and 2,140 nm), suggesting the presence of low-Ca pyroxene rather than the intermediate to high-Ca pyroxene detected in the mare units. The Mons Rümker pyroxene component is closer in composition to the older, western maria in composition (intermediate-Ca pyroxene). The Mairan T dome, Mons Rümker, and the highlands in Montes Jura have higher average reflectance values than the mare units, which may indicate the presence of a less mafic component, such as silica or feldspar, which cannot easily be detected in the VNIR domain when mixed with pyroxene (e.g., Adams & McCord, 1972; Pieters, 1986).

3.4. Geologic Units

Fourteen geologic units were defined and mapped in this study, including seven mare units (Im1, Im2, Im3, Em1, Em2, Em3, and Em4), three Rümker plateau units (IR1, IR2, and IR3), one nonmare highland units (Ith), and three dome units (Id, sd, and Idm; Figure 11). In order to define the geologic units, we followed the assumption by Hiesinger et al. (2000) that spectrally and compositionally homogeneous units are formed within a short period and each unit represents a single volcanic eruptive phase. Therefore, each spectrally and compositionally homogeneous unit is regarded as a geologic unit. We used TiO_2 and FeO contents and a false color composite from Kaguya MI data to define spectral and compositional units. The boundaries revealed by TiO_2 and FeO abundance data (Figure 9) correlate well with those revealed by M^3 color composite data (Figure 10). Boundaries are shown as black lines in Figure 11 and black dashed lines in Figure 9.

Crater size-frequency distribution methods were carried out to analyze the homogeneous units using TC Morning Map data to determine their absolute model ages. The results are shown in Table 1 together with optical maturity values, TiO_2 and FeO contents, and their uncertainties (shown as standard deviation). The cumulative crater frequency plots are shown in Figure 12. Mons Rümker was mapped, and surface ages were determined by Zhao et al. (2017), and we used their results in this study.

Im1, Im2, and Im3 are Imbrian-aged mare units (referred to as western maria above), adopting the lunar stratigraphy system by Stöffler and Ryder (2001). Im1 is the oldest mare unit (~3.42 Ga) in the area. It is dark bluish-purple in color with a red hue in the false color map (Figure 11), dominated by low-Ti basalts (2.4 wt %, mean content of TiO_2). Im2 (~3.39 Ga) is the largest mare unit in the area, containing five large craters (>3 km in diameter), Eratosthenian-aged Pythagoras secondaries, and large wrinkle ridges. It is orange-red in the

Table 1
Geologic Units in the Study Area

Unit	Area (km^2)	Model age (this study)[a] (Ga)	Hiesinger et al.[b] (2003) (Ga)	OMAT[cf]	TiO_2[df] (wt %)	FeO[df] (wt %)
Em4	35,905	1.21 (+0.03/−0.03)	1.33, P58	0.173 (0.023)	4.8 (1.2)	16.7 (0.7)
Em3	5,396	1.51 (+0.07/−0.07)		0.168 (0.023)	3.6 (0.9)	16.2 (0.7)
Em2	915	2.13 (+0.13/−0.13)		0.164 (0.033)	1.6 (0.4)	16.2 (0.6)
Em1	3,928	2.30 (+0.10/−0.10)		0.169 (0.029)	2.4 (0.5)	16.8 (0.4)
Im3	3,454	3.16 (+0.06/−0.09)	3.40, P13	0.184 (0.028)	1.4 (0.4)	15.3 (0.7)
Im2	44,327	3.39 (+0.02/−0.02)	3.44, P10	0.166 (0.035)	1.3 (0.4)	15.6 (0.8)
Im1	13,749	3.42 (+0.02/−0.02)	3.47, P9	0.166 (0.030)	2.4 (0.6)	16.3 (0.6)
IR3	747	3.51 (+0.04/−0.06)[e]		0.156 (0.025)	1.9 (0.4)	15.9 (0.8)
IR2	727	3.58 (+0.03/−0.04)[e]		0.155 (0.019)	1.5 (0.4)	14.9 (0.8)
IR1	2,912	3.71 (+0.04/−0.05)[e]		0.157 (0.027)	2.0 (0.6)	15.1 (1.0)

[a]Absolute model ages. Absolute model ages of each unit were calculated using CraterstatsII (http://www.geo.fu-berlin.de/). Uncertainties are reported by Michael and Neukum (2010). [b]Geologic units and their model ages defined by Hiesinger et al. (2003). [c]Mean optical maturity (OMAT) values. OMAT values were obtained from Kaguya MI data, using the method described by Lucey et al. (2000) and Lemelin et al. (2016). [d]Mean TiO_2 and FeO contents. [e]The CSFD results by Zhao et al. (2017). [f]The values in parentheses of OMAT, TiO_2, and FeO indicate standard deviation values of each unit.

false color map (Figure 11), and the TiO_2 content (1.3 wt %, mean content) is apparently lower than that of Im1. Im3 is located in the northeast near Louville P crater (~3.16 Ga; Figure 11), with a low TiO_2 content (1.4 wt %, mean content). It is the smallest Imbrian-aged unit in the area, embaying some of the highlands near Louville P. Most of the unit is covered by NE-orientated Pythagoras secondary ejecta, resulting in the largest OMAT value (0.184) in the area. Our mapping results of Imbrian-aged mare units correlate well with previous stratigraphic studies by Whitford-Stark and Head (1980) and Hiesinger et al. (2003).

Em1, Em2, Em3, and Em4 (Em3 and Em4 are referred to as eastern maria above) are Eratosthenian-aged mare units. Em1 (~2.30 Ga) embays Mons Rümker in the southwest. It has similar color ratios and TiO_2 contents as the neighboring unit, Im1, but it is different in its relatively high FeO contents and lower crater density. Em2 (~2.13 Ga) has the lowest TiO_2 contents (1.6 wt %, mean content) among the Eratosthenian units. It has an orange-red hue in the false color map (Figure 11) similar to the Im2 unit, but it has fewer craters and a younger model age. Em3 (~1.51 Ga) is located to the east of Mons Rümker. It is purple in the false color map (Figure 11), characterized by a low-Ti composition (3.6 wt %, mean content of TiO_2). This unit embays a portion of Mons Rümker in the east.

Em4 (~1.21 Ga) is the youngest mare unit in the area. This unit has a high TiO_2 (6–7%) content, except for the areas covered by Copernican-aged secondary ejecta, as discussed in section 3.2.1. The FeO contents of Em4 are also high (16.7 wt %, mean). This unit is purple-blue in the false color map (Figure 11) and embays dozens of highland kipukas. The wrinkle ridges are smaller than those of western maria, trending NE along the outer ring of the Imbrium basin. Rima Sharp incises this unit at its boundary with Montes Jura.

IR1, IR2, and IR3 are Rümker plateau units, according to the definition and crater counting results of Zhao et al. (2017) (Table 1). IR1 (~3.71 Ga) is a lineated terrain in the north of Mons Rümker, formed by a mixing of Iridum crater ejecta and basaltic materials. IR2 (~3.58 Ga) occurs northeast of Mons Rümker, exhibiting lower TiO_2 contents. IR3 (~3.51 Ga) covers the main portion of Mons Rümker, characterized by higher TiO_2 and FeO contents than IR2 (Zhao et al., 2017).

Three dome units are identified in the area. Two of them (ld, ~3.5 Ga; sd, active until ~3.0 Ga) were defined by Zhao et al. (2017) on the basis of their flank slopes. The silica-rich domes including the East Dome and the Mairan domes (ldm) are mapped as another independent unit with a highland volcanism formation mechanism in the Imbrian Period (Head & McCord, 1978).

Kipukas/highlands are informally defined as massif materials (Wilhelms, 1970) that resemble the Alpes Formation (Page, 1970), interpreted to have been formed by the ejecta of the Imbrium basin in previous studies (Scott & Eggleton, 1973; Spudis et al., 1988). In the current study, we defined it as the Ith unit after Scott and Eggleton (1973). It is the oldest unit in the area, contemporary with the Imbrium basin impact (~3.93 Ga; Snape et al., 2016).

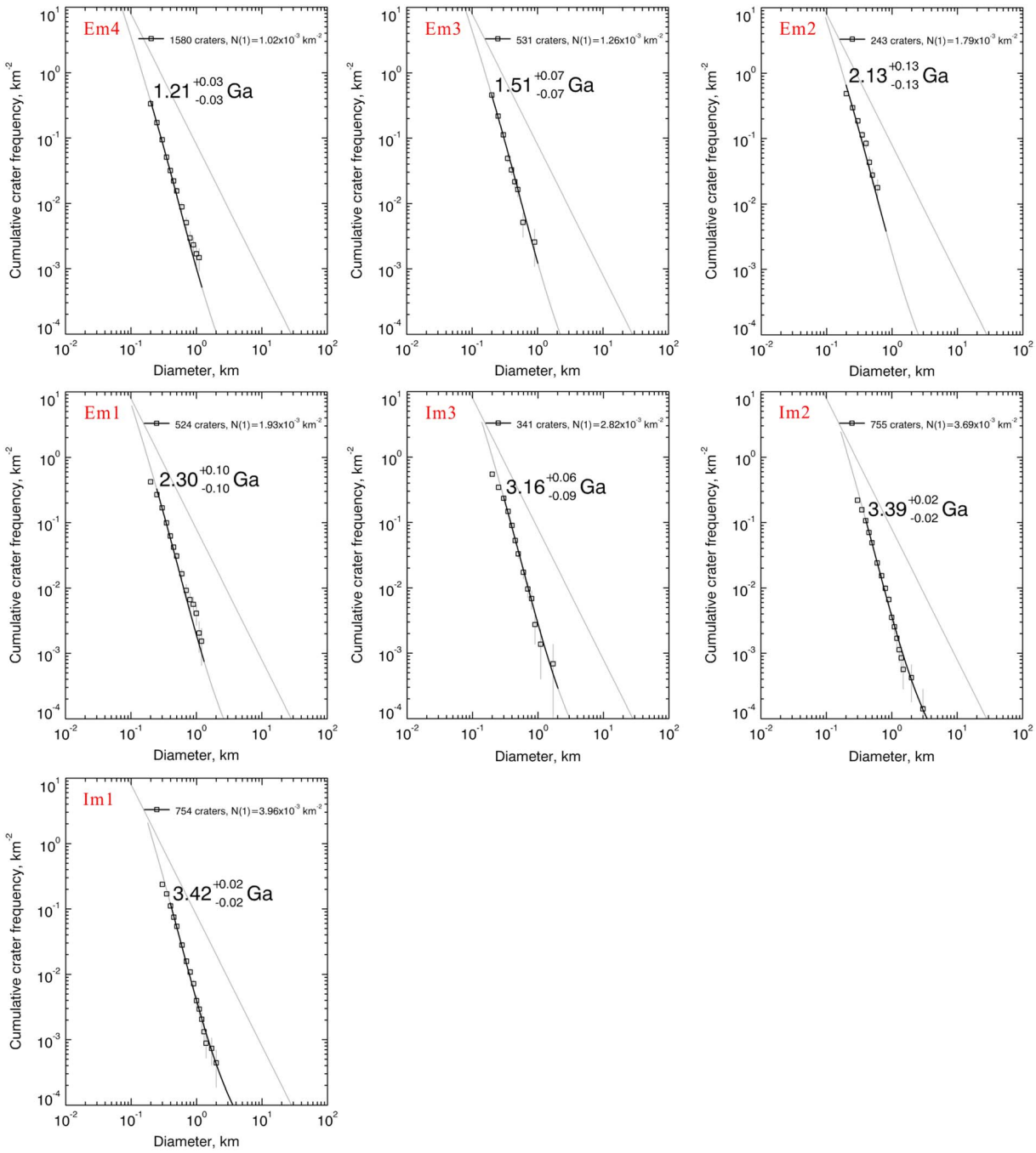

Figure 12. Cumulative crater frequency plots and absolute model ages of the mare units analyzed. See Table 1 for details. The lunar production function and the chronology function are given by Neukum et al. (2001).

4. Discussion

4.1. Volcanic Events and Geologic History

4.1.1. Volcanic Events

The oldest recognizable mare basaltic unit in Oceanus Procellarum is the Repsold Formation (medium to high TiO_2 content). At present it is only exposed in northwestern Oceanus Procellarum near the Rümker region (Whitford-Stark & Head, 1980). It is inferred to be beneath the uppermost mare basalts defined in this study, on the basis of superposition relationships and its extensive coverage (Whitford-Stark & Head, 1980). The

Repsold Formation was emplaced around 3.75 ± 0.05 Ga (Boyce & Jonnson, 1978) or 3.72 Ga (P28; Hiesinger et al., 2003, 2011) ago.

The basaltic unit IR1 formed ~3.71 Ga during the same period or shortly after the emplacement of the Repsold Formation, followed by IR2 (3.58 Ga) and IR3 (3.51 Ga; Zhao et al., 2017). Shallow domes (Id) formed around 3.5 Ga ago (Zhao et al., 2017). Extrusive steep-sided domes formed later by relatively high viscosity magma, and volcanic activity continued until ~3.0 Ga ago (Zhao et al., 2017). The basaltic eruptions in the Mons Rümker region are similar to the western maria flows in elemental composition (low TiO_2), mineralogy (intermediate pyroxene composition), and emplacement ages (Imbrian-aged), suggesting that they may be from the same mantle source region but have different eruption styles.

Although the small silica-rich East Dome has not been dated in this study due to its small area, it most likely formed in the Imbrian Period, contemporary with the Mairan domes (Head & McCord, 1978) and other silica-rich domes, for example, the Gruithuisen domes (3.7–3.85 Ga, Wagner et al., 2002) and the Hansteen domes (3.65–3.74 Ga, Wagner et al., 2010). On the other hand, its relatively shallow slopes (9°), low thorium abundance (8.6 ppm), and lower silica content compared with other Mairan domes (Glotch et al., 2011) might indicate that it is not completely similar to typical red spots that are formed by more viscous, silica-rich magmas (Glotch et al., 2010, 2011; Head & Wilson, 2017; Ivanov et al., 2016; Wilson & Head, 2003).

The Imbrian-aged mare basalts (Im1, Im2, and Im3) defined in the current study comprise the major mare eruption phase during the Late Imbrian Period (3.2–3.8 Ga; Hiesinger et al., 2000, 2003, 2010, 2011). This eruption phase has a very low-Ti to low-Ti and intermediate pyroxene composition (e.g., pigeonite), suggesting early magma source regions without ilmenite. The materials excavated from the largest crater (Harding D, 6.3 km diameter) have similar mineral, TiO_2, and FeO contents as those in the surface of the mare, unlike the underlying Repsold Formation materials, as do other impact craters. This implies that the thickness of the Imbrian mare units is at least 700 m. The sources of the Imbrian-aged basalt units are hard to trace, but the sinuous rilles in Mons Rümker and Aristarchus regions were probably the source of some of these materials (Whitford-Stark & Head, 1980).

The Eratosthenian-aged mare basalts (Em1, Em2, Em3, and Em4) represent the young phase of volcanism, characterized by high titanium content (Blewett et al., 1997; Elphic, 2002; Pieters, 1978) and high olivine content (Pieters, 1978; Staid et al., 2011; Staid & Pieters, 2001; Zhang et al., 2016). The Eratosthenian-aged mare basalts in this area are also rich in iron, especially the Em3 and Em4 units. The Em1 and Em2 units are not as high in TiO_2 and FeO content as the early Late Eratosthenian Period aged Em3 and Em4 units. The spectra from these units have band center positions shifted toward shorter wavelengths from Em3 to Em4 (Figure 10d), suggesting a slight change in the pyroxene compositions (decrease of calcium) of the eruptive high-Ti mare basalts with time.

Em4 comprises the main member of the Eratosthenian mare units in the area. Rima Sharp is the longest sinuous rille on the Moon and feeds most of the lavas of Em4 from the north in Sinus Roris with the assistance of Rima Mairan from the southeast (Whitford-Stark & Head, 1980). The Em4 lava flow boundaries are undetectable in WAC low solar illumination image data, although Eratosthenian-aged lava flow fronts can be readily observed in Mare Imbrium (Chen et al., 2018; Wu et al., 2018). This observation suggests that the Em4 lava flow unit thickness is too small to be recognized. Spectroscopic observations by M^3 show that materials excavated by craters with diameter greater than 900 m in the eastern maria (Em3 and Em4) are different from surface materials associated with Em3 and Em4 and similar to the older western maria. This observation indicates that the eastern Eratosthenian-aged mare units (Em3 and Em4) are superposed on the old western Imbrian-aged mare units (Im1, Im2, and Im3). Thus, we estimated the thickness of the eastern mare basalt to be less than 90 m using depth/diameter relationships (Pike, 1974). Further constraints on basalt thickness were provided by crater penetrating measurements (Thomson et al., 2009), yielding a thickness of 50–100 m for the young basalts (Em3 and Em4; Table 2), comparable to the 30–60 m estimated by Hiesinger et al. (2002).

In summary, the Imbrian-aged and Eratosthenian-aged mare units in the study area have a significant variation in age, mineralogy, composition, and volume, which are interpreted to originate from different mantle source regions or depths (Kato et al., 2017; Staid et al., 2011).

Table 2
Basalt Thickness of the Young Mare Units (Em3 and Em4) and Craters Used to Calculate the Thickness

No	Latitude (°)	Longitude (°)	Diameter (km)	*Dt* (km)	R_{base} (km)	H_b (m)
1	40.9	50.8	6.1	5.1	5.0	228 (±105)
2	42.1	52.2	1.6	1.4	0.9	119 (±7)
3	40.3	52.8	4.3	3.6	4.4	78 (±78)
4	39.8	53.2	2.0	1.7	1.4	106 (±22)
5	42.6	54.1	1.7	1.4	1.7	50 (±39)
6	43.2	55.5	1.2	1.0	0.7	97 (±3)
7	42.1	55.6	1.8	1.5	1.0	137 (±5)
8	42.3	56.0	3.3	2.8	2.6	132 (±53)

Note. The method applied is described in Thomson et al. (2009). *Dt* is the transient crater diameter. R_{base} is the radius of ejecta. H_b is the basalt thickness obtained. The error comes from the measurement of R_{base}.

4.1.2. Geological History

The sequence of geologic events in the area, including volcanic activity, tectonism (wrinkle ridge formation), and impact cratering, are now summarized. A geologic map (Figure 13) was produced, and we interpret the geological evolutionary history of the Rümker region as follows:

1. The Imbrium impact at 3.92 Ga ago generated a complex multiring system (Snape et al., 2016) and the outer ring materials formed the Ith unit in the area (Scott & Eggleton, 1973; Spudis et al., 1988). Ejecta

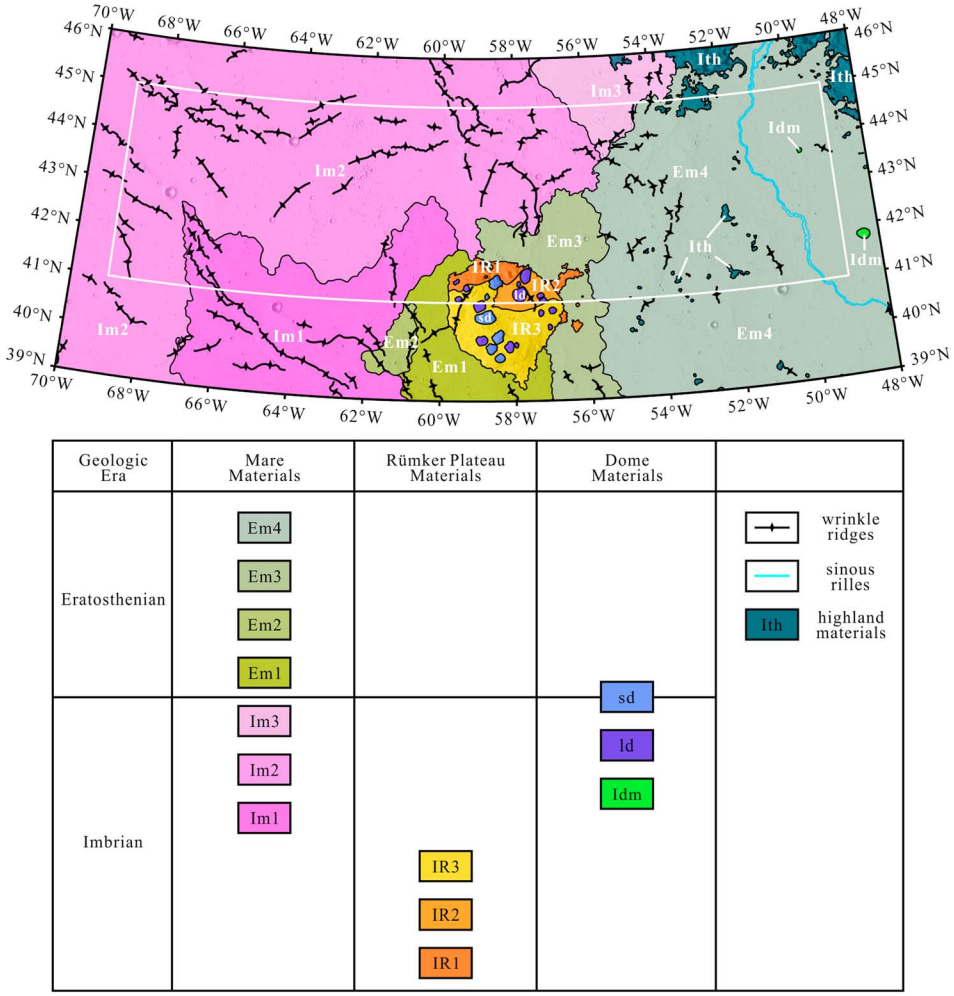

Figure 13. Geologic map of the Rümker region in northern Oceanus Procellarum.

of the Iridum impact (3.84–3.7 Ga; Wagner et al., 2002) formed the lineated terrain in the north of Mons Rümker before 3.71 Ga (Zhao et al., 2017).
2. The earliest detectable basaltic volcanism in the area erupted around 3.72 Ga ago (Hiesinger et al., 2003), forming medium to high-titanium mare basalts belonging to the Repsold Formation (Whitford-Stark & Head, 1980).
3. Basaltic volcanism was active from 3.71 to 3.51 Ga ago in Mons Rümker, forming plateau basalts IR1 (3.71 Ga), IR2 (3.58 Ga), and IR3 (3.51 Ga; Zhao et al., 2017).
4. Silica-rich domes (Idm) formed contemporaneously to, or a little earlier than, Mons Rümker by silica/felsite volcanic activity (Glotch et al., 2010, 2011; Head & McCord, 1978; Head & Wilson, 2017; Ivanov et al., 2016; Wilson & Head, 2003).
5. The major phase of basaltic volcanism occurred during the Late Imbrian Period, forming very low-Ti to low-Ti mare basalts (Im1, 3.42 Ga; Im2, 3.39 Ga; Im3, 3.16 Ga).
6. NW-oriented wrinkle ridges in Oceanus Procellarum were tectonically generated around 3.35 Ga ago (Yue et al., 2017).
7. The youngest phase of mare volcanism started at ~2.30 Ga ago and ceased at ~1.21 Ga ago, forming four episodes of mare units (Em1, 2.30 Ga; Em2, 2.13 Ga; Em3, 1.51 Ga; Em4, 1.21 Ga). The youngest mare volcanism (with elevated titanium content) formed the Em4 unit.

4.2. Potential Science Outcomes From Sample Return

Laboratory studies of lunar samples from Apollo and Luna missions (landing sites shown in Figures 1 and 2) solved numerous fundamental scientific issues of selenology and heralded the beginning of a golden age of lunar research that continues to this day (e.g., Hiesinger, 2006; Jaumann et al., 2012; Neal, 2009; Taylor, 2014; Taylor et al., 2006). However, most of the Moon remains unexplored and there are still many unanswered scientific questions (National Research Council, 2007) that remain to be addressed by returned samples (e.g., Crawford et al., 2007, 2012; Crawford & Joy, 2014; Flahaut et al., 2012; Kring & Durda, 2012). China's CE5 lunar sample return mission to the Rümker region provides a great opportunity to solve some of the significant outstanding questions of lunar science. Samples from each geologic unit in the area have specific scientific importance, which should be ranked to maximize the science outcomes.

4.2.1. The Young Mare Units

On the Moon, the phase of mare basalt volcanism that records internal mantle evolution began (cryptomaria; Whitten & Head, 2015) prior to the end of impact basin formation (Oriental basin, ~3.68 Ga; Whitten et al., 2011) peaked between 3 and 4 Ga and subsequently declined with time, with only a few extrusive mare basalt deposits, widely spaced in the last 50% of the lunar history (Head & Wilson, 2017; Hiesinger et al., 2000, 2003, 2010, 2011; Morota et al., 2011). Where is the youngest mare basalt volcanism, what is its exact radiometric age, and what does its mineralogy and geochemistry tell us about the lunar mantle in the last half of lunar history?

Remote sensing data and counts of superposed impact craters on mare basalt units show that the youngest mare basalts could be as young as 1.2 Ga (Hiesinger et al., 2003, 2011). The youngest mare basalts are concentrated in the northern Oceanus Procellarum region, centrally located in the PKT, characterized by elevated abundances of radioactive heat-producing elements such as U, Th, and K (e.g., Haskin, 1998; Jolliff et al., 2000; Prettyman et al., 2006).

One (P58, 1.33 Ga) of the five young mare units (others are P56, P57, P59, and P60) occurs in the Rümker region (Hiesinger et al., 2003, 2011). P58 nearly corresponds with Em3 (1.51 Ga) and Em4 (1.21 Ga) in the current study. These two mare units have extremely young model ages, especially Em4, which is one of the youngest mare units on the Moon revealed by crater counting methods (Hiesinger et al., 2000, 2003, 2010, 2011; Morota et al., 2011). These high-Ti basalts (Em3 and Em4) are younger than any existing lunar samples, including the youngest lunar meteorites (NWA032, 2.8 Ga; Fagan et al., 2002).

These factors led scientists to place the return of samples from these young mare basalt units as a top priority for future lunar exploration (National Research Council, 2007). Analysis of these samples in Earth laboratories will (1) provide exact radiometric dates for the extrusive events and thereby improve our knowledge of lunar chronology, (2) provide new knowledge of the nature of the geochemistry and mineralogy of basaltic source regions and their isotopic and trace element characteristics, (3) permit the testing of the role of the radioactive PKT in the generation of late-stage mare volcanism, and (4) improve understanding of the thermal state

of the lunar interior in late lunar history, thereby testing and constraining models for the thermal evolution of the Moon.

Finally, the ages of these young basalts are currently determined by impact CSFD of the craters superposed on the units, calibrated by counts of craters on geologic units radiometrically dated in Earth laboratories from samples collected by Apollo and Luna missions. However, no samples have currently been returned from such young lunar units, and, thus, there is a high level of uncertainty in the size-frequency distribution ages in the last half of lunar impact chronology (Crawford et al., 2007; Stöffler et al., 2006; Stöffler & Ryder, 2001). Return of samples from these young basalts would thus serve to provide an absolute calibration for the cratering flux, an accomplishment that will assist in our understanding of the geological evolution of planetary bodies throughout the Solar System (Crawford et al., 2007; Kring & Durda, 2012; National Research Council, 2007).

4.2.2. Other Geological Units

The Imbrian-aged mare basalts in the area are low-Ti (Im1) to very low-Ti (Im2 and Im3) and dominated by intermediate composition pyroxene such as pigeonite. Samples from the Imbrian-aged mare basalts are similar in age (Imbrian-aged) and composition (very low-Ti to low Ti) to Apollo and Luna samples (Apollo 12 and 15 missions collected low-Ti basalts, and Apollo 17 and Luna 24 missions collected very low-Ti basalts). Samples from these units can provide important ground truth to help evaluate the low-Ti and VLT basalt petrogenesis models (Neal & Taylor, 1992) and reveal mantle source region properties (Snyder et al., 1992).

Steep-sided lunar domes and volcanic complexes have not been sampled in previous lunar missions. Samples from the domes on Mons Rümker and the silica-rich East Dome can reveal the elemental and mineral compositions of these surface materials, providing ground truth for remote sensing data/methods. Geochemical analysis can constrain the nature of magma source regions and test the existing models and mechanism of dome formation (Head & Wilson, 2017; Wilson & Head, 2003; Wilson & Head, 2017). Samples from the silica-rich East Dome can reveal the nature of silica-rich volcanism on the Moon, the effects of thorium concentration on red spot formation, and lead to further understanding of the late stage magmatic evolution of the Moon (Glotch et al., 2010, 2011; Hagerty et al., 2006).

4.3. Proposed Sampling Sites

Comparing the potential science return of each of the geologic units, we suggest that the Em4 unit has the richest scientific value and should be the top priority landing unit for the CE5 mission. Sampling anywhere in the Em4 unit could return young mare materials and fulfill the desired scientific goals. Thus, we propose the entire Em4 unit as a candidate from which to choose a specific landing site (proposed landing site A). Our suggestion to land in the young mare unit is supported by Ling et al. (2017) and Jolliff et al. (2017).

Furthermore, sampling the regolith developed on the Em4 unit could readily return samples of the underlying older materials (i.e., Imbrian-aged mare basalts) excavated by impacts. In addition, the secondary clusters and crater rays in the area indicate that material in the soils is likely to contain admixed ejecta from distant craters, such as Copernicus, Harpalus, and Pythagoras. Finally, ejecta from craters superposed on the exposed kipukas in the Em4 unit may provide fragments from the underlying Imbrium basin ejecta unit. In contrast, landing in the western maria is likely to return only the Imbrian-aged mare deposits and possible ejecta and fragments (similar in age and composition to Apollo and Luna samples) that could also be sampled in Em4 unit.

Mons Rümker and the silica-rich East Dome are also valuable sampling units of significant scientific interest. We list these as the second and third priority landing sites for the CE5 mission and propose two landing sites within each unit (proposed landing sites B and C). Proposed landing site B is at a steep-sided dome on Mons Rümker (centered at 58.53°W, 41.41°N). This steep-sided dome is ~7.5 km in diameter. The top of this dome is flat and may be suitable for landing ($<2°$). The third proposed landing site is on the silica-rich East Dome (centered at 49.85°W, 43.68°N), which is discussed in detail in sections 3.2.4 and 4.1.1.

These three proposed landing sites (Figure 14 and Table 3) can be further evaluated to assess the engineering requirements (e.g., surface slopes, rock abundance, and crater density) in a future study.

4.4. Engineering Advantages of Sampling the Em4 Unit

The proposed landing site A (Em4) is not only the very highest scientific priority but also very favorable from an engineering and landing safety point of view. It offers a relatively safe landing site, which is

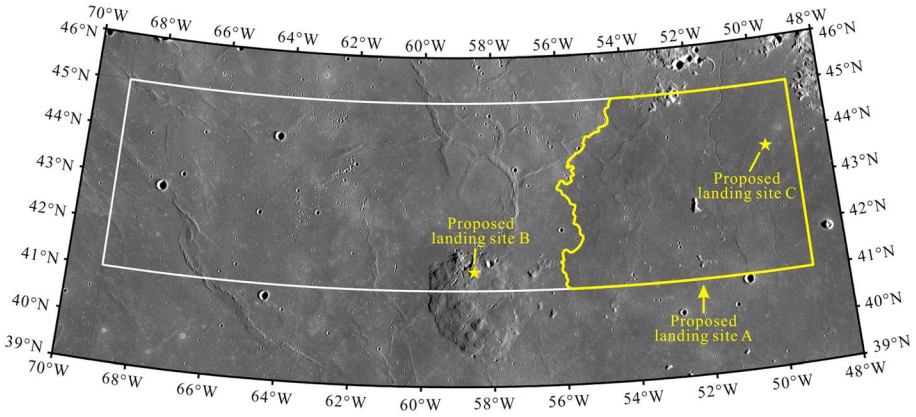

Figure 14. The location of proposed landing sites in this study. Landing site A indicates the region of the Em4 mare unit.

regionally flat, young, and is really homogeneous and so does not require pin-point landing. These benefits are listed:

1. The Em4 unit is regionally flat (1.1°, mean slope) and very similar to the topography and slopes observed at the CE3 landing site. CE3 landing data can be used to simulate the nature of the landing region.
2. The Em4 unit is very young (1.21 Ga), which means it contains fewer large impact craters and has smoother topography.
3. The Em4 unit is very widely distributed and continuous in the CE5 landing region (Figures 11 and 14), making up almost one third of the total landing region. Landing and sampling anywhere in the Em4 unit would fulfill the primary scientific objectives of the mission.
4. The Em4 unit is a mare unit very similar in age and surface characteristics to that explored by CE3 (Qiao et al., 2014; Zhao et al., 2014) and suited for soft landing by CE5. Ground penetrating radar data from the CE3 landing site (Fa et al., 2015; Xiao et al., 2015; Yuan et al., 2017; Zhang et al., 2015) show the type of vertical structure to be expected in the CE5 Em4 unit.

Table 3
Proposed Landing Sites and Their Scientific Values

Landing site	Center coordinates	Unit	Local feature	Scientific values
A	Em4	Em4	Young mare	1. Unsampled new rock type 2. Extent of lunar volcanism duration 3. Properties of late stage lunar volcanism 4. Deep mantle properties 5. Concentration mechanism of Th and its role in late stage volcanism 6. Precise isotopic age of young volcanism 7. Impact cratering flux history 8. Improving CSFD dating method and chronology
B	58.53°W, 41.41°N	sd	Mons Rümker	1. Origin of lunar domes 2. Property of the magma source 3. The duration of Mons Rümker volcanism 4. Impact cratering flux history 5. Improve CSFD dating method and chronology
C	49.85°W, 43.68°N	ldm	Silica dome	1. Rock-type characteristic of the dome 2. Origin of the silica-rich domes 3. Properties of the magma source 4. Evolution of magmas 5. Influence of Th in silica dome formation 6. The mechanism of Th concentration

5. Conclusions

We systematically studied the topography, geomorphology, composition, and surface properties of the Rümker region, the target region for the CE5 sample return mission. Principle results include the following:

1. The Rümker region is an unexplored and unsampled area in northern Oceanus Procellarum. It is located within the unusual PKT, characterized by levels of high heat producing elements.
2. Fourteen geologic units were defined and mapped, including seven mare units (Im1, Im2, Im3, Em1, Em2, Em3, and Em4), three Rümker plateau units (IR1, IR2, and IR3), one nonmare highland units (Ith), and three dome units (Id, sd, and Idm).
3. The Rümker region experienced long (~3.7 to ~1.2 Ga) and complex volcanic activity, forming multiple volcanic units with distinct composition and mineralogy.
4. Three candidate landing sites are proposed for the CE5 mission. We interpret the Em4 unit (proposed landing site A) to be the most scientifically valuable and also the safest from a landing and engineering point of view and should be listed as the top priority for the CE5 mission.

Acknowledgments

This study is supported by the National Natural Science Foundation of China (41772050 and 41773061), the Fundamental Research Funds for the Central Universities, and the China University of Geosciences, Wuhan (CUGL160402 and CUG2017G02), MOST Special Fund from the State Key Laboratory of Geological Processes and Mineral Resources, China University of Geosciences (MSFGPMR05). Wang is supported by the National Natural Science Foundation of China (11502277). The work of Flahaut is supported by the CNES (Luna/ExoMars APR). Martinot is supported by the Netherlands Organization for Scientific Research (NWO) grant. The Kaguya TC Morning Map data, TC DTM data, and Multiband Imager (MI) data are available from the SELENE Data Archive (http://darts.isas.jaxa.jp/planet/pdap/selene/). The LRO WAC Data and NAC data are available from the LROC website (http://lroc.sese.asu.edu/). The LOLA and Kaguya TC merged hillshade map are available from USGS Astrogeology Science Center (https://astrogeology.usgs.gov/). The M^3 Level 2 data are archived in the Planetary Data System. Spectra for lunar minerals are available from RELAB reference library (http://www.planetary.brown.edu/relab/). The thorium abundance data by Prettyman et al. (2006) are available from the Planetary Data System Geoscience Node (http://pds-geosciences.wustl.edu/lunar/lp-l-grs-5-elem-abundance-v1/). The crater counting files (.scc) are in Data Set S1 in the supporting information. Crater counting was carried using CraterTools (Kneissl et al., 2011). Statistics on CSFD based on crater counting files (.scc) were performed on CraterstatsII (Michael & Neukum, 2010). CraterTools, CraterstatsII, and the introduction on how to use these software are available from http://www.geo.fu-berlin.de/en/geol/fachrichtungen/planet/software/index.html. The geologic map of the Rümker region (Figure 13) has been uploaded individually to Figure S1 in the supporting information.

References

Adams, J. B. (1974). Visible and near-infrared diffuse reflectance spectra of pyroxenes as applied to remote sensing of solid objects in the solar system. *Journal of Geophysical Research*, *79*, 4829–4836. https://doi.org/10.1029/JB079i032p04829

Adams, J. B., & McCord, T. B. (1972). Electronic spectra of pyroxenes and interpretation of telescopic spectral reflectivity curves of the Moon. Proceedings of 3rd Lunar Science Conference, 3 (pp. 3021–3024).

Barker, M. K., Mazarico, E., Neumann, G. A., Zuber, M. T., Haruyama, J., & Smith, D. E. (2016). A new lunar digital elevation model from the Lunar Orbiter Laser Altimeter and SELENE Terrain Camera. *Icarus*, *273*, 346–355. https://doi.org/10.1016/j.icarus.2015.07.039

Besse, S., Sunshine, J., Staid, M., Boardman, J., Pieters, C., Guasqui, P., et al. (2013). A visible and near-infrared photometric correction for Moon Mineralogy Mapper (M^3). *Icarus*, *222*(1), 229–242. https://doi.org/10.1016/j.icarus.2012.10.036

Blewett, D. T., Lucey, P. G., Hawke, B. R., & Jolliff, B. L. (1997). Clementine images of the lunar sample-return stations: Refinement of FeO and TiO_2 mapping techniques. *Journal of Geophysical Research*, *102*, 16,319–16,325. https://doi.org/10.1029/97JE01505

Boardman, J. W., Pieters, C. M., Green, R. O., Lundeen, S. R., Varanasi, P., Nettles, J., et al. (2011). Measuring moonlight: An overview of the spatial properties, lunar coverage, selenolocation, and related level 1B products of the Moon Mineralogy Mapper. *Journal of Geophysical Research*, *116*, E00G14. https://doi.org/10.1029/2010JE003730

Boroughs, L. L., & Spudis, P. D. (2001). *The stratigraphy of lava flows in northern Oceanus Procellarum, Moon*. Paper Presented at 32nd Lunar and Planetary Science Conference, Lunar and Planetary Institute, Houston.

Boyce, J. M., & Jonnson, D. A. (1978). Ages of flow units in the far eastern maria and implications for basin-filling history. Proceedings of 9th Lunar and Planetary Science Conference (pp. 2717–2728).

Burns, R. G., Vaughan, D. J., Abu-Eid, R. M., Witner, M., & Morawski, A. (1973). Spectral evidence for Cr^{3+}, Ti^{3+}, Fe^{2+} rather than Cr^{2+} and Fe^{3+} in lunar ferromagnesian silicates. Proceedings of 4th Lunar Science Conference, 1 (pp. 983-994).

Campbell, B. A., Hawke, B. R., & Campbell, D. B. (2009). Surface morphology of domes in the Marius Hills and Mons Rümker regions of the Moon from Earth-based radar data. *Journal of Geophysical Research*, *114*, E01001. https://doi.org/10.1029/2008JE003253

Chen, Y., Li, C., Ren, X., Liu, J., Wu, Y., Lu, Y., et al. (2018). The thickness and volume of young basalts within Mare Imbrium. *Journal of Geophysical Research: Planets*, *123*, 630–645. https://doi.org/10.1002/2017JE005380

Clark, R. N., Pieters, C. M., Green, R. O., Boardman, J. W., & Petro, N. E. (2011). Thermal removal from near-infrared imaging spectroscopy data of the Moon. *Journal of Geophysical Research*, *116*, E00G16. https://doi.org/10.1029/2010JE003751

Cloutis, E. A., & Gaffey, M. J. (1991). Pyroxene spectroscopy revisited: Spectral-compositional correlations and relationship to geothermometry. *Journal of Geophysical Research*, *96*(E5), 22,809–22,826. https://doi.org/10.1029/91JE02512

Coman, E. O., Joliff, B. L., & Carpenter, P. (2018). Mineralogy and chemistry of Ti-bearing lunar soils: Effects on reflectance spectra and remote sensing observations. *Icarus*, *306*, 243–255. https://doi.org/10.1016/j.icarus.2018.02.008

Crawford, I. A., Anand, M., Cockell, C. S., Falcke, H., Green, D. A., Jaumann, R., & Wieczorek, M. A. (2012). Back to the Moon: The scientific rationale for resuming lunar surface exploration. *Planetary and Space Science*, *74*(1), 3–14. https://doi.org/10.1016/j.pss.2012.06.002

Crawford, I. A., Fagents, S., & Joy, K. (2007). Full Moon exploration. *Astronomy & Geophysics*, *48*, 3.18–3.21. https://doi.org/10.1111/j.1468-4004.2007.48318.x

Crawford, I. A., & Joy, K. H. (2014). Lunar exploration: Opening a window into the history and evolution of the inner solar system. *Philosophical Transactions of the Royal Society A*, *372*(2024), 20130315. https://doi.org/10.1098/rsta.2013.0315

Dmitrovsky, A. A., Zacharova, M. A., & Slyuta, E. N. (2017). *Preliminary data on the age of the Mons Rumker Volcanic Province*. Paper Presented at 48th Lunar and Planetary Science Conference, Lunar and Planetary Institute, The Woodlands.

Eliason, E. M., McEwen, A. S., Robinson, M. S., Lee, E. M., Becker, T., Gaddis, L., et al. (1999). *Digital processing for a global multispectral map of the Moon from the Clementine UVVIS Imaging Instrument*. Paper presented at 30th Lunar and Planetary Science Conference, Lunar and Planetary Institute, Houston.

Elphic, R. C. (2002). Lunar Prospector Neutron Spectrometer constraints on TiO_2. *Journal of Geophysical Research*, *107*(E4), 5024. https://doi.org/10.1029/2000JE001460

Fa, W., Zhu, M.-H., Liu, T., & Plescia, J. B. (2015). Regolith stratigraphy at the Chang'E-3 landing site as seen by lunar penetrating radar. *Geophysical Research Letters*, *42*, 10,179–10,187. https://doi.org/10.1002/2015GL066537

Fagan, T. J., Taylor, G. J., Keil, K., Bunch, T. E., Wittke, J. H., Korotev, R. L., et al. (2002). Northwest Africa 032: Product of lunar volcanism. *Meteoritics & Planetary Science*, *37*(3), 371–394. https://doi.org/10.1111/j.1945-5100.2002.tb00822.x

Farrand, W. H., Kramer, G. Y., Gaddis, L. R., & Videen, G. (2015). *Spectral and photometric examination of pyroclastic mantles over Mons Rumker*. Paper Presented at 46th Lunar and Planetary Science Conference, Lunar and Planetary Institute, The Woodlands.

Fischer, E. M., & Pieters, C. M. (1994). Remote determination of exposure degree and iron concentration of lunar soils using VIS-NIR spectroscopic methods. *Icarus*, *111*(2), 475–488. https://doi.org/10.1006/icar.1994.1158

Flahaut, J., Blanchette-Guertin, J.-F., Jilly, C., Sharma, P., Souchon, A., van Westrenen, W., & Kring, D. A. (2012). Identification and characterization of science-rich landing sites for lunar lander missions using integrated remote sensing observations. *Advances in Space Research*, *50*(12), 1647–1665. https://doi.org/10.1016/j.asr.2012.05.020

Glotch, T. D., Hagerty, J. J., Lucey, P. G., Hawke, B. R., Giguere, T. A., Arnold, J. A., et al. (2011). The Mairan domes: Silicic volcanic constructs on the Moon. *Geophysical Research Letters*, *38*, L21204. https://doi.org/10.1029/2011GL049548

Glotch, T. D., Lucey, P. G., Bandfield, J. L., Greenhagen, B. T., Thomas, I. R., Elphic, R. C., et al. (2010). Highly silicic compositions on the Moon. *Science*, *329*(5998), 1510–1513. https://doi.org/10.1126/science.1192148

Green, R. O., Pieters, C., Mouroulis, P., Eastwood, M., Boardman, J., Glavich, T., et al. (2011). The Moon Mineralogy Mapper (M^3) imaging spectrometer for lunar science: Instrument description, calibration, on-orbit measurements, science data calibration and on-orbit validation. *Journal of Geophysical Research*, *116*, E00G19. https://doi.org/10.1029/2011JE003797

Hagerty, J. J., Lawrence, D. J., Hawke, B. R., Vaniman, D. T., Elphic, R. C., & Feldman, W. C. (2006). Refined thorium abundances for lunar red spots: Implications for evolved, nonmare volcanism on the Moon. *Journal of Geophysical Research*, *111*, E06002. https://doi.org/10.1029/2005JE002592

Haruyama, J., Matsunaga, T., Ohtake, M., Morota, T., Honda, C., Yokota, Y., et al. (2008). Global lunar-surface mapping experiment using the Lunar Imager/Spectrometer on SELENE. *Earth, Planets and Space*, *60*(4), 243–255. https://doi.org/10.1186/bf03352788

Haruyama, J., Ohtake, M., Matsunaga, T., Otake, H., Ishihara, Y., Masuda, K., et al. (2014). *Data products of SELENE (Kaguya) Terrain Camera for future lunar missions*. Paper presented at 45th Lunar and Planetary Science Conference, Lunar and Planetary Institute, The Woodlands.

Haskin, L. A. (1998). The Imbrium impact event and the thorium distribution at the lunar highlands surface. *Journal of Geophysical Research*, *103*, 1679–1689. https://doi.org/10.1029/97JE03035

Haskin, L. A., Gillis, J. J., Korotev, R. L., & Jolliff, B. L. (2000). The materials of the lunar Procellarum KREEP Terrane: A synthesis of data from geomorphological mapping, remote sensing, and sample analyses. *Journal of Geophysical Research*, *105*, 20,403–20,415. https://doi.org/10.1029/1999JE001128

Head, J. W. (1977). Regional distribution of Imbrium Basin deposits: Relationship to pre-Imbrian topography and mode of emplacement. In The Imbrium Consortium (Ed.), *Interdisciplinary studies by the Imbrium Consortium* (pp. 120–125). Cambridge: The Imbrium Consortium.

Head, J. W. (1982). Lava flooding of ancient planetary crusts: Geometry, thickness, and volumes of flooded lunar impact basins. *The Moon and the Planets*, *26*(1), 61–88. https://doi.org/10.1007/bf00941369

Head, J. W., & Gifford, A. (1980). Lunar mare domes: Classification and modes of origin. *The Moon and the Planets*, *22*(2), 235–258. https://doi.org/10.1007/bf00898434

Head, J. W., & McCord, T. B. (1978). Imbrian-age highland volcanism on the Moon: The Gruithuisen and Mairan domes. *Science*, *199*(4336), 1433–1436. https://doi.org/10.1126/science.199.4336.1433

Head, J. W., & Wilson, L. (2017). Generation, ascent and eruption of magma on the Moon: New insights into source depths, magma supply, intrusions and effusive/explosive eruptions (part 2: Predicted emplacement processes and observations). *Icarus*, *283*, 176–223. https://doi.org/10.1016/j.icarus.2016.05.031

Hiesinger, H. (2006). New views of lunar geoscience: An introduction and overview. *Reviews in Mineralogy and Geochemistry*, *60*(1), 1–81. https://doi.org/10.2138/rmg.2006.60.1

Hiesinger, H., Head, J. W., Wolf, U., Jaumann, R., & Neukum, G. (2002). Lunar mare basalt flow units: Thicknesses determined from crater size-frequency distributions. *Geophysical Research Letters*, *29*(8), 1248. https://doi.org/10.1029/2002GL014847

Hiesinger, H., Head, J. W., Wolf, U., Jaumann, R., & Neukum, G. (2003). Ages and stratigraphy of mare basalts in Oceanus Procellarum, Mare Nubium, Mare Cognitum, and Mare Insularum. *Journal of Geophysical Research*, *108*(E7), 5056. https://doi.org/10.1029/2002JE001985

Hiesinger, H., Head, J. W., Wolf, U., Jaumann, R., & Neukum, G. (2010). Ages and stratigraphy of lunar mare basalts in Mare Frigoris and other nearside maria based on crater size-frequency distribution measurements. *Journal of Geophysical Research*, *115*, E03003. https://doi.org/10.1029/2009JE003380

Hiesinger, H., Head, J. W., Wolf, U., Jaumann, R., & Neukum, G. (2011). Ages and stratigraphy of lunar mare basalts: A synthesis. *Geological Society of America Special Papers*, *477*, 1–51. https://doi.org/10.1130/2011.2477(01

Hiesinger, H., Jaumann, R., Neukum, G., & Head, J. W. (2000). Ages of mare basalts on the lunar nearside. *Journal of Geophysical Research*, *105*, 29,239–29,275. https://doi.org/10.1029/2000JE001244

Horgan, B. H. N., Cloutis, E. A., Mann, P., & Bell, J. F. (2014). Near-infrared spectra of ferrous mineral mixtures and methods for their identification in planetary surface spectra. *Icarus*, *234*, 132–154. https://doi.org/10.1016/j.icarus.2014.02.031

Hurwitz, D. M., Head, J. W., & Hiesinger, H. (2013). Lunar sinuous rilles: Distribution, characteristics, and implications for their origin. *Planetary and Space Science*, *79-80*, 1–38. https://doi.org/10.1016/j.pss.2012.10.019

Hurwitz, D. M., Head, J. W., Wilson, L., & Hiesinger, H. (2012). Origin of Lunar Sinuous Rilles: Modeling effects of gravity, surface slope, and lava composition on erosion rates during the formation of Rima Prinz. *Journal of Geophysical Research*, *117*, E00H14. https://doi.org/10.1029/2011JE004000

Ivanov, M. A., Head, J. W., & Bystrov, A. (2016). The lunar Gruithuisen silicic extrusive domes: Topographic configuration, morphology, ages, and internal structure. *Icarus*, *273*, 262–283. https://doi.org/10.1016/j.icarus.2015.12.015

Jaumann, R., Hiesinger, H., Anand, M., Crawford, I. A., Wagner, R., Sohl, F., et al. (2012). Geology, geochemistry, and geophysics of the Moon: Status of current understanding. *Planetary and Space Science*, *74*(1), 15–41. https://doi.org/10.1016/j.pss.2012.08.019

Jolliff, B. L., Gillis, J. J., Haskin, L. A., Korotev, R. L., & Wieczorek, M. A. (2000). Major lunar crustal terranes: Surface expressions and crust-mantle origins. *Journal of Geophysical Research*, *105*, 4197–4216. https://doi.org/10.1029/1999JE001103

Jolliff, B. L., Wang, A., Ling, Z., & Zhang, J. (2017). *Scientific context and objectives for Chang'E-4 and Chang'E-5 missions*. Paper Presented at the 3rd Beijing International Forum on Lunar and Deep-Space Exploration, Chinese Academy of Sciences, Beijing, China.

Kato, S., Morota, T., Yamaguchi, Y., Watanabe, S., Otake, H., & Ohtake, M. (2017). Magma source transition of lunar mare volcanism at 2.3 Ga. *Meteoritics & Planetary Science*, *52*(9), 1899–1915. https://doi.org/10.1111/maps.12896

Kneissl, T., Gasselt, S. v., & Neukum, G. (2011). Map-projection-independent crater size-frequency determination in GIS environments—New software tool for ArcGIS. *Planetary and Space Science*, *59*(11-12), 1243–1254. https://doi.org/10.1016/j.pss.2010.03.015

Kreslavsky, M. A., Head, J. W., Neumann, G. A., Rosenburg, M. A., Aharonson, O., Smith, D. E., & Zuber, M. T. (2013). Lunar topographic roughness maps from Lunar Orbiter Laser Altimeter (LOLA) data: Scale dependence and correlation with geologic features and units. *Icarus*, *226*(1), 52–66. https://doi.org/10.1016/j.icarus.2013.04.027

Kring, D. A., & Durda, D. D. (Eds.) (2012). *A Global Lunar Landing Site study to provide the scientific context for exploration of the Moon*. Houston: Lunar and Planetary Institute.

Laneuville, M., Wieczorek, M. A., Breuer, D., & Tosi, N. (2013). Asymmetric thermal evolution of the Moon. *Journal of Geophysical Research: Planets*, *118*, 1435–1452. https://doi.org/10.1002/jgre.20103

Lawrence, D. J., Feldman, W. C., Barraclough, B. L., Binder, A. B., Elphic, R. C., Maurice, S., et al. (2000). Thorium abundances on the lunar surface. *Journal of Geophysical Research*, *105*(E8), 20,307–20,331. https://doi.org/10.1029/1999JE001177

Lawrence, S. J., Stopar, J. D., Hawke, B. R., Greenhagen, B. T., Cahill, J. T. S., Bandfield, J. L., et al. (2013). LRO observation of morphology and surface roughness of volcanic cones and lobate lava flows in the Marius Hills. *Journal of Geophysical Research: Planets*, *118*, 615–634. https://doi.org/10.1002/jgre.20060

Lemelin, M., Lucey, P. G., Gaddis, L. R., Hare, T., & Ohtake, M. (2016). *Global map products from the Kaguya Multiband Imager at 512 ppd: Minerals, FeO, and OMAT*. Paper Presented at 47th Lunar and Planetary Science Conference, Lunar and Planetary Institute, The Woodlands.

Ling, Z., Jolliff, B. L., Wang, A., Li, C., Liu, J., Zhang, J., et al. (2015). Correlated compositional and mineralogical investigations at the Chang'e-3 landing site. *Nature Communications*, *6*(1), 8880. https://doi.org/10.1038/ncomms98805

Ling, Z., Liu, C., Jolliff, B. L., Zhang, J., Li, B., Sun, L., Chen, J., et al. (2017). *Spectral and mineralogical analysis of Chang'E-5 candidate landing site in northern Oceanus Procellarum*. Paper presented at 48th Lunar and Planetary Science Conference, Lunar and Planetary Institute, The Woodlands.

Lucey, P. G., Blewett, D. T., Taylor, G. J., & Hawke, B. R. (2000). Imaging of lunar surface maturity. *Journal of Geophysical Research*, *105*, 20,377–20,386. https://doi.org/10.1029/1999JE001110

Martinot, M., Besse, S., Flahaut, J., Quantin-Nataf, C., Lozac'h, L., & Westrenen, W. v. (2018). Mineralogical diversity and geology of Humboldt crater derived using Moon Mineralogy Mapper data. *Journal of Geophysical Research: Planets*, *123*, 612–629. https://doi.org/10.1002/2017JE005435

Maxwell, T. A., El-Baz, F., & Ward, S. H. (1975). Distribution, morphology, and origin of ridges and arches in Mare Serenitatis. *Geological Society of America Bulletin*, *86*(9), 1273–1278. https://doi.org/10.1130/0016-7606(1975)86%3C1273:DMAOOR%3E2.0.CO;2

Michael, G. G., & Neukum, G. (2010). Planetary surface dating from crater size-frequency distribution measurements: Partial resurfacing events and statistical age uncertainty. *Earth and Planetary Science Letters*, *294*(3–4), 223–229. https://doi.org/10.1016/j.epsl.2009.12.041

Morota, T., Haruyama, J., Ohtake, M., Matsunaga, T., Honda, C., Yokota, Y., et al. (2011). Timing and characteristics of the latest mare eruption on the Moon. *Earth and Planetary Science Letters*, *302*(3–4), 255–266. https://doi.org/10.1016/j.epsl.2010.12.028

Mustard, J. F., Pieters, C. M., Isaacson, P. J., Head, J. W., Besse, S., Clark, R. N., et al. (2011). Compositional diversity and geologic insights of the Aristarchus crater from Moon Mineralogy Mapper data. *Journal of Geophysical Research*, *116*, E00G12. https://doi.org/10.1029/2010JE003726

National Research Council (2007). *The scientific context for exploration of the Moon*. Washington DC: National Academies Press.

Neal, C. R. (2009). The Moon 35 years after Apollo: What's left to learn? *Chemie der Erde - Geochemistry*, *69*(1), 3–43. https://doi.org/10.1016/j.chemer.2008.07.002

Neal, C. R., & Taylor, L. A. (1992). Petrogenesis of mare basalts: A record of lunar volcanism. *Geochimica et Cosmochimica Acta*, *56*(6), 2177–2211. https://doi.org/10.1016/0016-7037(92)90184-k

Neukum, G., Ivanov, B. A., & Hartmann, W. K. (2001). Cratering records in the inner solar system in relation to the lunar reference system. *Space Science Reviews*, *96*(1/4), 55–86. https://doi.org/10.1023/A:1011989004263

Ohtake, M., Haruyama, J., Matsunaga, T., Yokota, Y., Morota, T., & Honda, C. (2008). Performance and scientific objectives of the SELENE (KAGUYA) Multiband Imager. *Earth, Planets and Space*, *60*(4), 257–264. https://doi.org/10.1186/bf03352789

Otake, H., Ohtake, M., & Hirata, N. (2012). *Lunar iron and titanium abundance algorithms based on SELENE (Kaguya) Multiband Imager data*. Paper Presented at 43rd Lunar and Planetary Science Conference, Lunar and Planetary Institute, The Woodlands.

Page, N. J. (1970). *Geologic map of the Cassini quadrangle of the Moon (Map I-666)*. Flagstaff: USGS Astrogeology Science Center.

Pieters, C. M. (1978). Mare basalt types on the front side of the Moon—A summary of spectral reflectance data. Preceedings of 9th Lunar and Planetary Science Conference (pp. 2825–2849).

Pieters, C. M. (1986). Composition of the lunar highland crust from near-infrared spectroscopy. *Reviews of Geophysics*, *24*, 557–578. https://doi.org/10.1029/RG024i003p00557

Pieters, C. M., Boardman, J., Buratti, B., Chatterjee, A., Clark, R., Glavich, T., et al. (2009). The Moon Mineralogy Mapper (M^3) on Chandrayaan-1. *Current Science*, *96*(4), 500–505.

Pieters, C. M., Staid, M. I., Fischer, E. M., Tompkins, S., & He, G. (1994). A sharper view of impact craters from Clementine data. *Science*, *266*(5192), 1844–1848. https://doi.org/10.1126/science.266.5192.1844

Pike, R. J. (1974). Depth/diameter relations of fresh lunar craters: Revision from spacecraft data. *Geophysical Research Letters*, *1*, 291–294. https://doi.org/10.1029/GL001i007p00291

Prettyman, T. H., Hagerty, J. J., Elphic, R. C., Feldman, W. C., Lawrence, D. J., McKinney, G. W., & Vaniman, D. T. (2006). Elemental composition of the lunar surface: Analysis of gamma ray spectroscopy data from Lunar Prospector. *Journal of Geophysical Research*, *111*, E12007. https://doi.org/10.1029/2005JE002656

Qiao, L., Xiao, L., Zhao, J., Huang, Q., & Haruyama, J. (2014). Geological features and evolution history of Sinus Iridum, the Moon. *Planetary and Space Science*, *101*, 37–52. https://doi.org/10.1016/j.pss.2014.06.007

Robinson, M. S., Brylow, S. M., Tschimmel, M., Humm, D., Lawrence, S. J., Thomas, P. C., et al. (2010). Lunar Reconnaissance Orbiter Camera (LROC) instrument overview. *Space Science Reviews*, *150*(1–4), 81–124. https://doi.org/10.1007/s11214-010-9634-2

Rosenburg, M. A., Aharonson, O., Head, J. W., Kreslavsky, M. A., Mazarico, E., Neumann, G. A., et al. (2011). Global surface slopes and roughness of the Moon from the Lunar Orbiter Laser Altimeter. *Journal of Geophysical Research*, *116*, E02001. https://doi.org/10.1029/2010JE003716

Sato, H., Robinson, M. S., Lawrence, S. J., Denevi, B. W., Hapke, B., Joliff, B. L., & Hiesinger, H. (2017). Lunar mare TiO_2 abundances estimated from UV/Vis reflectance. *Icarus*, *296*, 216–238. https://doi.org/10.1016/j.icarus.2017.06.013

Scholten, F., Oberst, J., Matz, K. D., Roatsch, T., Wählisch, M., Speyerer, E. J., & Robinson, M. S. (2012). GLD100: The near-global lunar 100 m raster DTM from LROC WAC stereo image data. *Journal of Geophysical Research*, *117*, E00H17. https://doi.org/10.1029/2011JE003926

Scott, D. H., & Eggleton, R. E. (1973). *Geologic map of the Rümker quadrangle of the Moon (Map I805)*. Flagstaff: USGS Astrogeology Science Center.

Scott, D. H., McCauley, J. F., & West, M. N. (1977). *Geologic map of the west side of the Moon (Map I-1034)*. Flagstaff: USGS Astrogeology Science Center.

Sharpton, V. L., & Head, J. W. (1988). Lunar mare ridges: Analysis of ridge-crater intersections and implications for the tectonic origin of mare ridges. Proceedings of 18th Lunar and Planetary Science Conference (pp. 307–317).

Smith, E. I. (1973). Identification, distribution and significance of lunar volcanic domes. *The Moon*, *6*(1-2), 3–31. https://doi.org/10.1007/bf02630650

Smith, E. I. (1974). Rümker hills: A lunar volcanic dome complex. *The Moon*, *10*(2), 175–181. https://doi.org/10.1007/bf00655718
Snape, J. F., Nemchin, A. A., Grange, M. L., Bellucci, J. J., Thiessen, F., & Whitehouse, M. J. (2016). Phosphate ages in Apollo 14 breccias: Resolving multiple impact events with high precision U-Pb SIMS analyses. *Geochimica et Cosmochimica Acta*, *174*, 13–29. https://doi.org/10.1016/j.gca.2015.11.005
Snyder, G. A., Taylor, L. A., & Neal, C. R. (1992). A chemical model for generating the sources of mare basalts: Combined equilibrium and fractional crystallization of the lunar magmasphere. *Geochimica et Cosmochimica Acta*, *56*(10), 3809–3823. https://doi.org/10.1016/0016-7037(92)90172-F
Spudis, P. D., Hawke, B. R., & Lucey, P. G. (1988). Materials and formation of the Imbrium basin. Proceedings of 18th Lunar and Planetary Science Conference (pp. 155–168).
Staid, M. I., & Pieters, C. M. (2001). Mineralogy of the last lunar basalts: Results from Clementine. *Journal of Geophysical Research*, *106*, 27,887–27,900. https://doi.org/10.1029/2000JE001387
Staid, M. I., Pieters, C. M., Besse, S., Boardman, J., Dhingra, D., Green, R., et al. (2011). The mineralogy of late stage lunar volcanism as observed by the Moon Mineralogy Mapper on Chandrayaan-1. *Journal of Geophysical Research*, *116*, E00G10. https://doi.org/10.1029/2010JE003735
Stöffler, D., & Ryder, G. (2001). Stratigraphy and isotope ages of lunar geologic units: Chronological standard for the inner solar system. In R. Kallenbach, J. Geiss, & W. K. Hartmann (Eds.), *Chronology and evolution of Mars* (pp. 9–54). Dordrecht: Springer.
Stöffler, D., Ryder, G., Ivanov, B. A., Artemieva, N. A., Cintala, M. J., & Grieve, R. A. F. (2006). Cratering history and lunar chronology. *Reviews in Mineralogy and Geochemistry*, *60*(1), 519–596. https://doi.org/10.2138/rmg.2006.60.05
Strom, R. G. (1972). Lunar mare ridges, rings and volcanic ring complexes. In S. K. Runcorn & H. C. Urey (Eds.), *The Moon* (pp. 187–215). Dordrecht: Springer. https://doi.org/10.1007/978-94-010-2861-5_19
Taylor, S. R. (2014). The Moon re-examined. *Geochimica et Cosmochimica Acta*, *141*, 670–676. https://doi.org/10.1016/j.gca.2014.06.031
Taylor, S. R., Taylor, G. J., & Taylor, L. A. (2006). The Moon: A Taylor perspective. *Geochimica et Cosmochimica Acta*, *70*(24), 5904–5918. https://doi.org/10.1016/j.gca.2006.06.262
Thomson, B. J., Grosfils, E. B., Bussey, D. B. J., & Spudis, P. D. (2009). A new technique for estimating the thickness of mare basalts in Imbrium Basin. *Geophysical Research Letters*, *36*, L12201. https://doi.org/10.1029/2009GL037600
Wagner, R., Head, J. W., Wolf, U., & Neukum, G. (2002). Stratigraphic sequence and ages of volcanic units in the Gruithuisen region of the Moon. *Journal of Geophysical Research*, *107*(E11), 5104. https://doi.org/10.1029/2002JE001844
Wagner, R., Head, J. W., Wolf, U., & Neukum, G. (2010). Lunar red spots: Stratigraphic sequence and ages of domes and plains in the Hansteen and Helmet regions on the lunar nearside. *Journal of Geophysical Research*, *115*, E06015. https://doi.org/10.1029/2009JE003359
Wang, Q., & Xiao, L. (2017). *China's Lunar Exploration Programme*. Paper presented at Lunar Exploration Analysis 2017, Lunar and Planetary Institute, The Woodlands.
Weider, S. Z., Crawford, I. A., & Joy, K. H. (2010). Individual lava flow thicknesses in Oceanus Procellarum and Mare Serenitatis determined from Clementine multispectral data. *Icarus*, *209*(2), 323–336. https://doi.org/10.1016/j.icarus.2010.05.010
Whitford-Stark, J. L., & Head, J. W. (1977). The Procellarum volcanic complexes—Contrasting styles of volcanism. Proceedings of 8th Lunar Science Conference (pp. 2705–2724).
Whitford-Stark, J. L., & Head, J. W. (1980). Stratigraphy of Oceanus Procellarum basalts: Sources and styles of emplacement. *Journal of Geophysical Research*, *85*, 6579–6609. https://doi.org/10.1029/JB085iB11p06579
Whitten, J., Head, J. W., Staid, M., Pieters, C. M., Mustard, J., Clark, R., et al. (2011). Lunar mare deposits associated with the Orientale impact basin: New insights into mineralogy, history, mode of emplacement, and relation to Orientale Basin evolution from Moon Mineralogy Mapper (M^3) data from Chandrayaan-1. *Journal of Geophysical Research*, *116*, E00G09. https://doi.org/10.1029/2010JE003736
Whitten, J. L., & Head, J. W. (2015). Lunar cryptomaria: Physical characteristics, distribution, and implications for ancient volcanism. *Icarus*, *247*, 150–171. https://doi.org/10.1016/j.icarus.2014.09.031
Wieczorek, M. A., Neumann, G. A., Nimmo, F., Kiefer, W. S., Taylor, G. J., Melosh, H. J., et al. (2013). The crust of the Moon as seen by GRAIL. *Science*, *339*(6120), 671–675. https://doi.org/10.1126/science.1231530
Wieczorek, M. A., & Phillips, R. J. (2000). The "Procellarum KREEP Terrane": Implications for mare volcanism and lunar evolution. *Journal of Geophysical Research*, *105*, 20,417–20,430. https://doi.org/10.1029/1999JE001092
Wilhelms, D. E. (1970). *Summary of lunar stratigraphy—Telescopic observations (599F)*. Washington DC: United States Government Office.
Wilhelms, D. E., & McCauley, J. F. (1971). *Geologic map of the near side of the Moon (Map I-703)*. Flagstaff: Astrogeology Science Center.
Wilson, L., & Head, J. W. (2003). Lunar Gruithuisen and Mairan domes: Rheology and mode of emplacement. *Journal of Geophysical Research*, *108*(E2), 5012. https://doi.org/10.1029/2002JE001909
Wilson, L., & Head, J. W. (2017). Generation, ascent and eruption of magma on the Moon: New insights into source depths, magma supply, intrusions and effusive/explosive eruptions (part 1: Theory). *Icarus*, *283*, 146–175. https://doi.org/10.1016/j.icarus.2015.12.039
Wöhler, C., Lena, R., & Pau, K. C. (2007). *The lunar dome complex Mons Rümker: Morphometry, rheology, and mode of emplacement*. Paper Presented at 38th Lunar and Planetary Science Conference, Lunar and Planetary Institute, League City, USA.
Wu, Y., Li, L., Luo, X., Lu, Y., Chen, Y., Pieters, C. M., et al. (2018). Geology, tectonism and composition of the northwest Imbrium region. *Icarus*, *303*, 67–90. https://doi.org/10.1016/j.icarus.2017.12.029
Xiao, L. (2014). China's touch on the Moon. *Nature Geoscience*, *7*(6), 391–392. https://doi.org/10.1038/ngeo2175
Xiao, L., Zhu, P., Fang, G., Xiao, Z., Zou, Y., Zhao, J., et al. (2015). A young multilayered terrane of the northern Mare Imbrium revealed by Chang'E-3 mission. *Science*, *347*(6227), 1226–1229. https://doi.org/10.1126/science.1259866
Yuan, Y., Zhu, P., Zhao, N., Xiao, L., Garnero, E., Xiao, Z., et al. (2017). The 3-D geological model around Chang'E-3 landing site based on lunar penetrating radar channel 1 data. *Geophysical Research Letters*, *44*, 6553–6561. https://doi.org/10.1002/2017GL073589
Yue, Z., Li, W., Di, K., Liu, Z., & Liu, J. (2015). Global mapping and analysis of lunar wrinkle ridges. *Journal of Geophysical Research: Planets*, *120*, 978–994. https://doi.org/10.1002/2014JE004777
Yue, Z., Michael, G. G., Di, K., & Liu, J. (2017). Global survey of lunar wrinkle ridge formation times. *Earth and Planetary Science Letters*, *477*, 14–20. https://doi.org/10.1016/j.epsl.2017.07.048
Zeng, X., Zuo, W., Zhang, Z., Liu, Y., & Li, C. (2017). *Topographic and geologic analysis of the pre-selection landing sites for Chang'E 5 (CE-5) lunar sample returning mission of China*. Paper Presented at 19th EGU General Assembly, EGU, Vienna, Austria.
Zhang, J., Yang, W., Hu, S., Lin, Y., Fang, G., Li, C., et al. (2015). Volcanic history of the Imbrium basin: A close-up view from the lunar rover Yutu. *Proceedings of the National Academy of Sciences of the United States of America*, *112*(17), 5342–5347. https://doi.org/10.1073/pnas.1503082112
Zhang, X., Wu, Y., Ouyang, Z., Bugiolacchi, R., Chen, Y., Zhang, X., et al. (2016). Mineralogical variation of the late stage mare basalts. *Journal of Geophysical Research: Planets*, *121*, 2063–2080. https://doi.org/10.1002/2016JE005051

Zhao, J., Huang, J., Qiao, L., Xiao, Z., Huang, Q., Wang, J., et al. (2014). Geologic characteristics of the Chang'E-3 exploration region. *Science China - Physics Mechanics & Astronomy*, *57*(3), 569–576. https://doi.org/10.1007/s11433-014-5399-z

Zhao, J., Xiao, L., Qiao, L., Glotch, T. D., & Huang, Q. (2017). The Mons Rümker volcanic complex of the Moon: A candidate landing site for the Chang'E-5 mission. *Journal of Geophysical Research: Planets*, *122*, 1419–1442. https://doi.org/10.1002/2016JE005247

Zou, Y. L., & Li, W. (2017). *Scientific visions of lunar research-station from China*. Paper Presented at 48th Lunar and Planetary Science Conference, Lunar and Planetary Institute, The Woodlands.

Zou, Y. L., Xu, L., & Wang, Q. (2016). Progress in China's lunar exploration program. *Chinese Journal of Space Science*, *36*(5), 610–619. https://doi.org/10.11728/cjss2016.05.610